Depositional Environment and Lithofacies Analyses of Eocene Lacustrine Shale in the Bohai Bay Basin: Insights from Mineralogy and Elemental Geochemistry

Danish KHAN[1, 2], LIANG Chao[2, *], QIU Longwei[2, *], Kamran MIRZA[3], WANG Yelei[2], Muhammad KASHIF[4], Saif Ur REHMAN[3], WANG Yuzhe[2] and TENG Jianbin[2, 5]

[1] *State Key Laboratory of Ore Deposit Geochemistry, Institute of Geochemistry, Chinese Academy of Sciences, Guiyang 550081, China*
[2] *School of Geosciences, China University of Petroleum, Qingdao, Shandong 266580, China*
[3] *Institute of Geology, University of the Punjab, Lahore 54590, Pakistan*
[4] *Department of Earth Sciences, University of Sargodha, Sargodha 40100, Pakistan*
[5] *Shengli Oil Field, Dongying, Shandong 257015, China*

Abstract: The effect of various depositional parameters including paleoclimate, paleosalinity and provenance, on the depositional mechanism of lacustrine shale is very important in reconstructing the depositional environment. The classification of shale lithofacies and the interpretation of shale depositional environment are key features used in shale oil and gas exploration and development activity. The lower 3rd member of the Eocene Shahejie Formation (Es_3^x shale) was selected for this study, as one of the main prospective intervals for shale oil exploration and development in the intracratonic Bohai Bay Basin. Mineralogically, it is composed of quartz (avg. 9.6%), calcite (avg. 58.5%), dolomite (avg. 7%), pyrite (avg. 3.3%) and clay minerals (avg. 20%). An advanced methodology (thin-section petrography, total organic carbon and total organic sulfur contents analysis, X-ray diffraction (XRD), X-ray fluorescence (XRF), field-emission scanning electron microscopy (FE-SEM)) was adopted to establish shale lithofacies and to interpret the depositional environment in the lacustrine basin. Six different types of lithofacies were recognized, based on mineral composition, total organic carbon (TOC) content and sedimentary structures. Various inorganic geochemical proxies (Rb/Sr, Ca/(Ca + Fe), Ti/Al, Al/Ca, Al/Ti, Zr/Rb) have been used to interpret and screen variations in depositional environmental parameters during the deposition of the Es_3^x shale. The experimental results indicate that the environment during the deposition of the Es_3^x shale was warm and humid with heightened salinities, moderate to limited detrital input, higher paleohydrodynamic settings and strong oxygen deficient (reducing) conditions. A comprehensive depositional model of the lacustrine shale was developed. The interpretations deduced from this research work are expected to not only expand the knowledge of shale lithofacies classification for lacustrine fine-grained rocks, but can also offer a theoretical foundation for lacustrine shale oil exploration and development.

Key words: shale lithofacies, shale mineralogy, elemental geochemistry, depositional environment, Shahejie Formation, Bohai Bay Basin

Citation: Khan et al., 2023. Depositional Environment and Lithofacies Analyses of Eocene Lacustrine Shale in the Bohai Bay Basin: Insights from Mineralogy and Elemental Geochemistry. Acta Geologica Sinica (English Edition), 97(2): 589–609. DOI: 10.1111/1755-6724.14985

1 Introduction

The sedimentary environment is the key parameter of sedimentary facies that controls the behavior and distribution of shale lithofacies in a basin. The deposition of shale in lacustrine basins can record continental paleoclimatic conditions and the paleoenvironment (Smith and Carroll, 2015). Basins of lacustrine origin are relatively restricted and the paleoclimatic conditions in lacustrine basins may affect the equilibrium of the rates of evaporation and fresh water by driving agitations in the lake's hydrological conditions (Chamberlain et al., 2013; Ma et al., 2016). These agitations cause variations in lake water chemistry, productivity and terrigenous input, which ultimately affect the depositional processes in lacustrine basins (Graf et al., 2015; Smith and Carroll, 2015). The recent advancements in unconventional petroleum systems has led to a re-evaluation of the important geological processes that affect fine-grained sedimentary rocks (Jarvie, 2012; Taylor and Macquaker, 2014). The depositional processes that deposit shales and other fine-grained sedimentary rocks are very complicated (Han et al., 2021a). These processes can control both spatial and temporal distribution of rock properties, which are significant parameters in the exploration for source and reservoir rocks (Jarvie et al., 2007; Loucks et al., 2009, 2012; Charpentier and Cook, 2011; Andrews, 2013). For shale petroleum systems, extensive research has been

* Corresponding author. E-mail: liangchao0318@163.com; qiulwsd@163.com

http://www.geojournals.cn/dzxbcn/ch/index.aspx; https://onlinelibrary.wiley.com/journal/17556724

focused on marine shales (Abouelresh and Slatt, 2012; Kuhn et al., 2012; Liang et al., 2012; El Attar and Pranter, 2016; Fairbanks et al., 2016; Lü et al., 2020), while research on lacustrine shale is still in the early stages (Burton et al., 2014; Schenk et al., 2015). Research on carbonate-rich lacustrine shales is also less documented in the Zhanhua Depression (Liang et al., 2017; Han et al., 2021b).

The overall depositional style is the key parameter to interpret and characterize fine-grained sedimentary deposits (Lazar et al., 2015; Schieber, 2016; Sachsenhofer et al., 2017; Tao et al., 2017; Dodd et al., 2019; Song et al., 2020). Research into the character and distribution of shale lithofacies is fundamental for shale hydrocarbon exploration and production activities in China, because many shale hydrocarbon resources in the Chinese basins are very heterogeneous. Due to this heterogeneity, the distinctive shale reservoirs are very challenging to identify (He et al., 2016). The deposition of shale occurs in a variety of different and diverse depositional settings, which often mark changes in total organic carbon (TOC) contents, sedimentary structures and mineralogical composition (Yang et al., 2015). Shales and shale lithofacies are still under-characterized in Chinese basins, especially when compared with other parts of the world.

This study describes and details the results of a comprehensive investigation into TOC content, mineralogy, elemental geochemistry and sedimentary structures found within the Es_3^x shale in the study area. From this analysis, a detailed classification of shale lithofacies is proposed, which is based on the above-mentioned parameters. The prime focus of this research was to provide a simple classification and distribution of shale lithofacies and to elucidate the effect of the depositional environment on the evolution of shale lithofacies. The main objectives of the current research work are: (1) to interpret the depositional environment of the lacustrine shale, based on inorganic and organic geochemistry; (2) to analyze the depositional settings based on the mineral composition and sedimentary structures; and (3) to explain the effect of depositional environment on the evolution of lacustrine shale lithofacies. This study can be useful to provide a shale lithofacies scheme for lacustrine sediments and can be used globally by other researchers in similar sedimentary environments. The interpretations inferred from this study are expected to not only have the ability to expand the knowledge of shale lithofacies origins of lacustrine fine-grained rocks, but can also offer a theoretical basis for lacustrine shale oil exploration and development.

2 Geological Setting

The Bohai Bay Basin (BBB) is a rift-related intracontinental lacustrine basin located on the eastern coastline of China (Fig. 1). It covers an area of nearly 200,000 km^2. The BBB has been divided into two tectonic evolutionary stages i.e., the Paleogene syn-rift stage and the Neogene–Quaternary post-rift stage. The first stage can further be sub-divided into numerous episodes of rifting, such as the Paleocene–middle Eocene, the late Eocene and the Oligocene episodes. These episodes of rifting vary greatly among different depressions in this basin (Liu et al., 2022). The BBB is further divided into the Liaohe, Liaodong, Bozhong, Jiyang, Huanghua, Jizhong and Linqing sub-basins, from the northeast to southwestward sides (Huang et al., 2012; Khan et al., 2021, 2022). The Jiyang sub-basin is the area of interest for this research work. It is a typical rift-related sub-basin of the Mesozoic to Cenozoic eras, located in the southeastern part of the BBB (Hao et al., 2011; Zhu et al., 2013). It is further sub-divided into the Dongying, Zhanhua, Chezhen and Huimen depressions. There are various structural uplifts that separate these four depressions from each other, including the Yihezhuang, Chengdong and Chenjiazhuang uplifts (Fig. 1). Amongst these secondary depressions, the Zhanhua Depression is the area where our study well (Luo-69) is located, in the northeast of the Jiyang sub-basin. It covers an area of approximately 3610 km² and is located to the northwest of the Chenjiazhuang uplift, west of the Gudai uplift and south of the Chengdong and Yihezhuang uplifts (Jiu et al., 2013). It is confined by various faults, including the Gunan and Gubei faults on the east, the Yindong and Chengnan faults in the north, with the Shaojia and Yinan faults constraining its western sides (Fig. 1; Li et al., 2015, Khan et al., 2021).

The Zhanhua Depression has two stages of tectonic evolution, including the Eocene–Oligocene syn-rift stage and the Miocene–Pliocene post-rifting depression stage (Han et al., 2021a). The Zhanhua Depression evolved greatly due to these rifting stages and this ultimately affected the depositional characteristics of the studied basin. Stratigraphically, it contains Cenozoic strata, which unconformably overlie Mesozoic strata (Fig. 2a; Wang et al., 2005; Hao et al., 2009). The Dongying, Shahejie and Kongdian formations belong to the Cenozoic era, while the Guantao Formation and Minghuazhen Formation belong to the Neogene system (Fig. 2a). The Eocene Shahejie Formation, with its lacustrine origin, is the interval of interest for this study and it is extensively distributed thrpughout the Zhanhua Depression (Wang et al., 2005). It contains various discontinuous layers of oil shales, mudstones, sandstones, siltstones and evaporites, having been deposited in fluvio-lacustrine and deltaic depositional environments (Fig. 2a). The Shahejie Formation is further divided into four different members, including Es_1, Es_2, Es_3 and Es_4, Es_3 being further sub-divided into three sub-members, namely Es_3^x, Es_3^z and Es_3^s (Fig. 2a). This work focuses on the detailed interpretation of the first of these three sub-members, the Es_3^x shale member of the lacustrine Shahejie Formation (Jiu et al., 2013; Wang et al., 2015a). This shale member comprises a thick pile of organic-rich shale, calcareous shale, and dark-gray mudstone (Fig. 2b; Hu et al., 2001; Zhang et al., 2012; Jiu et al., 2013; Wang et al., 2015b; Liu et al., 2016).

3 Materials and Methods

A total of 43 core samples of the Es_3^x shale were collected from well Luo-69 in the study area. The

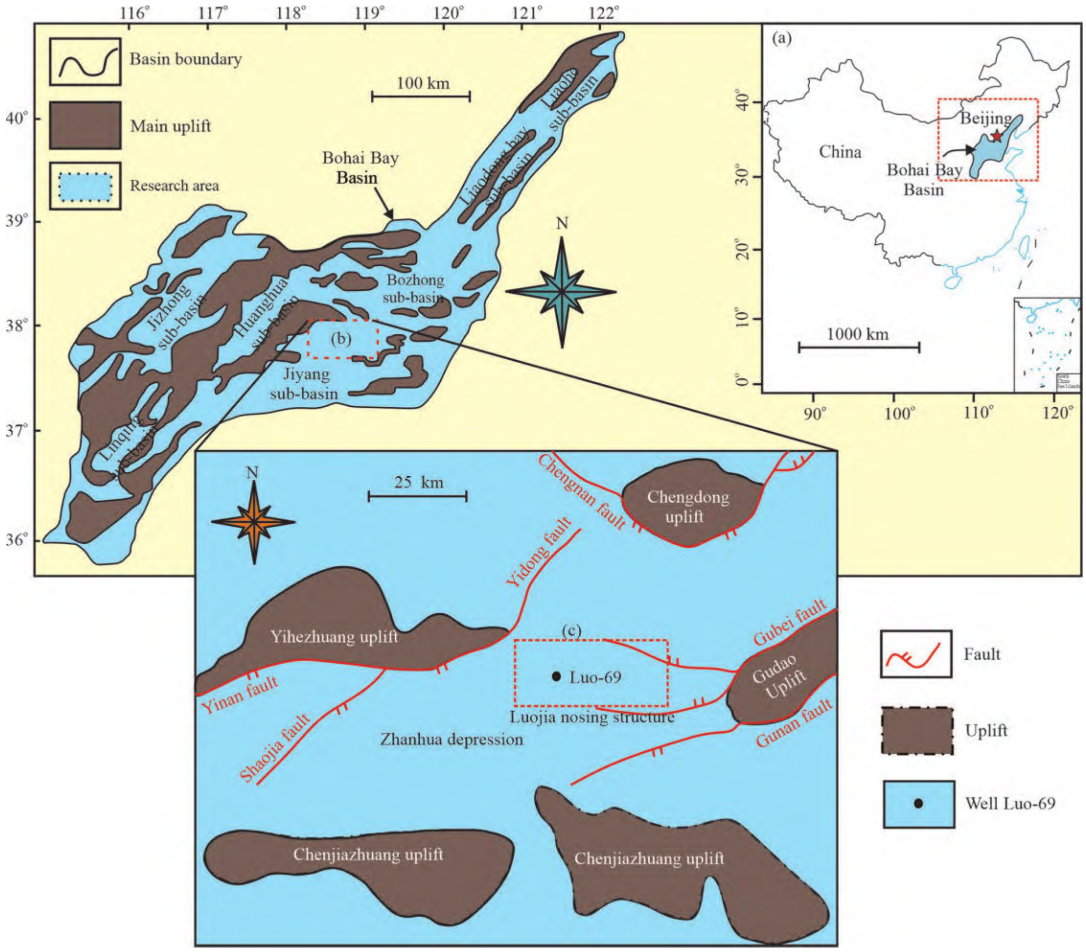

Fig. 1. Geological map showing the location of the study area (Zhanhua Depression) and the well location (modified from Ma et al., 2016).
(a) Map of China, showing the location of Bohai Bay Basin; (b) map of Bohai Bay Basin, showing the location of the Jiyang sub-basin; (c) map showing the location of well Luo-69 in the Zhanhua Depression.

representative samples were dried in a vacuum oven at 60 °C for 24 h to prepare them for the required experiments. The core samples chiefly comprised grayish to dark-gray calcareous shale. A total of 43 thin-sections were prepared from core samples for petrographic analysis of the shale. The thin-sections had 0.03 mm thickness and 22 mm × 22 mm area, according to the Chinese standards. A Leica DM4 polarizing microscope with × 100 objective lens magnification and 0.26 μm standard resolution was used to observe the thin-sections of the Es_3^x shale. The shale samples used for TOC analysis were crushed to a size less than 74 μm. Each sample of the Es_3^x shale weighing 0.135 g was added to a crucible and treated with diluted hydrochloric acid (HCl) for 24 h, in order to remove the inorganic carbonate contents. The HCl contaminants were then removed by treating samples with distilled water at 60°C temperature in an oven for 2 h. Organic geochemical analysis (TOC analysis) was performed on a LECO model CS744 to measure the concentration of total organic carbon (TOC) contents in the selected shale samples (a total of 29 Es_3^x shale samples). Additionally, total organic sulfur (TS) contents were also extracted from TOC analysis. The mineral composition of the studied shale samples has been identified using a PANalytical X'Pert Pro X-ray diffractometer, which was equipped with a copper X-ray target (40 kV, 40 mA). The identification of various mineral phases and their semi-quantitative relative abundances (wt%) were deduced by using computer diffractogram analysis, the different peaks being analyzed using LapSpec software. The shale samples were dried in an oven at 40°C for two days and then crushed to <44 μm size. Each shale sample weighing 5 g was placed in the X-ray diffractometer to identify different mineral phases and their relative amounts. The distribution of inorganic geochemical elements was identified by utilizing an X-ray fluorescence (XRF) spectrometer (model: M4 Tornado-Bruker). A voltage of 50 kV and 600 μA current were used as standard. A 25 μm beam size with a running time of 5 μs/pixel was used during this experiment. The concentration of inorganic geochemical elements was measured by using a total of 18 samples, which were placed in an XRF spectrometer. The shape, grain contact, behavior and distribution of different minerals in the Es_3^x shale samples have been observed by using a field-emission scanning electron microscope (FE-SEM). After detailed observation of mineral and elemental compositions, the Es_3^x shale samples with higher

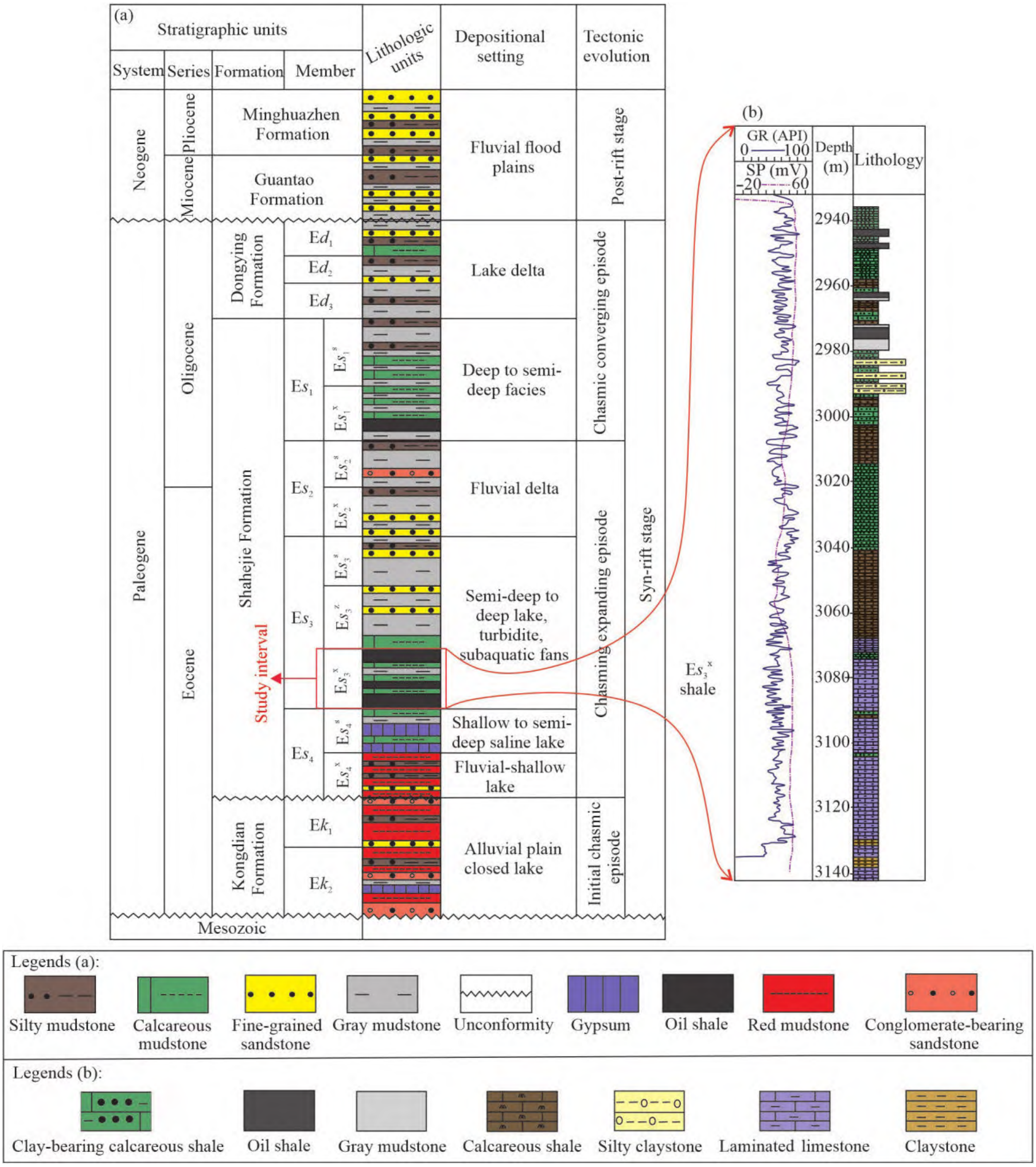

Fig. 2. (a) Stratigraphic column of the study area (Zhanhua Depression), the red box shows the study interval (Es_3^x shale); (b) gamma-ray and SP log against the lithology of the Es_3^x shale.

mineralogical heterogeneity were prepared for FE-SEM analysis. A total of 17 samples were selected for FE-SEM analysis in this study. Each shale sample was treated with argon ion polishing to improve the sample's smoothness, then treated with platinum to enhance conductivity. The argon ion-polished and platinum-coated core chips were placed in the Zeiss scanning electron microscope (model: Crossbeam-550-Gemini-2), coupled with EDS (energy disruptive system).

4 Results

4.1 Characteristics and distribution of different minerals

The results derived from XRD analysis indicate that the Es_3^x shale is dominated by calcareous minerals (calcite and dolomite) with sub-ordinate siliceous minerals (quartz and K-feldspar), pyrite and clay minerals. The mineralogy, TOC and total organic sulfur (TS) contents of each

Table 1 Whole-rock mineral composition, TOC content and TS of the Es_3^x shale in the Zhanhua Depression

Depth (m)	Whole-rock mineralogical composition (wt%) of the Es_3^x shale							TOC (wt%)	TS (wt%)
	Quartz	Feldspar	Calcite	Dolomite	Aragonite	Pyrite	Clay		
2937.8	12.2	0	6.8	3.8	49	11.2	17	6.56	1.85
2960.0	12.8	0	52.6	9.3	0	2.4	22.9	3.42	1.45
2990.05	9.6	0	53.7	6.9	0	3.4	26.4	2.36	2.13
2994.3	13	0	31.3	6.9	0	5.8	43	3.07	3.97
3012.2	11.9	0	53.6	5.4	0	4.9	24.2	4.41	2.37
3013.2	10.4	0	58.1	6.5	0	3.5	21.5	3.21	3.29
3016.3	14.3	0	37.3	6.9	0	5.4	36.1	3.79	3.81
3018.1	12.1	0	50.5	8.3	0	2.1	27	4.64	3.36
3023.8	14.2	0	38.4	10.1	0	5	32.3	5.19	3.6
3024.1	9.7	0	63.5	8.7	0	2.6	15.5	4.94	1.95
3033.5	11.9	0	42	10.6	0	3.1	32.4	5.83	3.7
3036.2	9.1	0	54.8	9.7	0	3.7	22.7	4.96	2.87
3038.0	11	1.1	52.6	8.5	0	3.1	23.7	3.99	2.22
3045.3	9.9	0	57.6	10.2	0	3.5	18.8	3.76	2.51
3052.5	8.2	0	64.7	7.8	0	1.4	17.9	6.44	2
3054.3	5.3	0	67.8	8.9	0	2.2	15.8	5.68	1.61
3056.43	8.9	0	67.6	6.1	0	2.6	14.8	5.7	2.03
3056.95	7.8	0	70.4	5.9	0	1.6	14.3	5.46	1.92
3063.0	8.4	0	71.2	4.2	0	1.8	14.4	1.83	1.75
3064.3	7.7	0	85.1	5.7	0	1.5	0	1.28	0.99
3067.8	5.6	0	75.6	8.2	0	2	8.6	2	1.57
3070.9	11.2	0	60.3	9.1	0	1.5	17.9	1.73	1.92
3090.7	6.7	0	65.8	7.3	0	1.9	18.3	1.65	1.97
3098.96	6.3	0	63.7	8.3	0	2.1	19.6	1.12	2.19
3100.68	9.5	0	62.6	7.6	0	2.2	18.1	1.62	2.6
3105.2	11.5	0	62.4	4.3	0	3.6	18	1.7	2.54
3110.2	7.5	0	73.5	3.1	0	1.4	14.5	1.27	1.9
3119.0	9	0	64.2	4.2	0	3.5	19.1	1.36	2.52
3140.25	11.9	0	50.1	2.7	0	4.5	29.4	1.53	5.46

representative Es_3^x shale sample are given in Table 1. The average percentages of quartz, calcite, dolomite, pyrite and clay minerals for the Es_3^x shale are 9.6%, 58.5%, 7%, 3.3% and 20%, respectively (Table 1). Clay to silt-sized quartz grains are randomly distributed, their concentration being higher in non-laminated shale intervals (Fig. 3a). The variation in quartz contents with increasing burial depth depends on the fluctuation of terrigenous input during deposition in the basin (Fig. 4). The Concentration of K-feldspar is very limited and restricted to only one sample (Fig. 3b). Calcite is the most commonly observed mineral in this basin and it is present in the form of micrite, sparite and fibrous calcite in the studied shale intervals (Fig. 3c, d). Micrite is abundant at shallow depths, while sparite and fibrous calcite are mostly encountered in depth intervals greater than 3000 m. Dolomite occurred in rhombohedral shape with random distribution in the studied shale samples (Fig. 3e, f). The contents of calcite and dolomite increase initially and then decrease with increasing burial depth in the study area (Fig. 4). Pyrite minerals generally occur in the form of framboids and euhedral pyrite, these pyrites being abundantly distributed throughout the Es_3^x shale intervals (Fig. 3g, h). The clay minerals are randomly distributed and their concentration increases with increasing burial depth in the study area (Figs. 3i, 4). The reason behind this fact is the variation in detrital input and later diagenetic events in the deeper parts of the basin.

4.2 Organic geochemistry

The Es_3^x shale is characterized by high TOC content ranges from 1.12 wt% to 6.56 wt% (avg. 3.49 wt%). TS content ranges from 0.99 wt% to 5.46 wt%, with an average content of 2.54 wt% in the Es_3^x shale (Fig. 4; Table 1). The change of TOC with increasing burial depth is due to the availability of biogenic contents in the basin. The concentration of biogenic contents largely depends on paleoclimatic conditions. The TOC content increases significantly at about 3030 m, because, at this depth, interval biogenic contents were abundantly encountered (Fig. 4).

4.3 Characteristics of sedimentary structures

During Es_3^x shale analysis, two types of sedimentary structures were commonly observed under the polarizing microscope i.e., syn-depositional sedimentary structures (parallel and lenticular or wavy laminations) (Fig. 5a, b) and post-depositional sedimentary structures (microfractures) (Fig. 5c–e). Hydrodynamic sorting of sedimentary particles creates a laminated fabric, with different laminations containing different mineralogical compositions (Fig. 5a, b). Microfractures are also observed during petrographic analysis of the Es_3^x shale. Microfractures are mostly filled with organic matter (OM) with sub-ordinate clay and siliceous minerals. These microfractures play a vital role in improving the reservoir properties of shale (Fig. 5c–e).

4.4 Distribution of major, minor and trace elements

The distribution and quantity of different inorganic geochemical elements (major, minor and trace) were measured using XRF spectrometers. The results of these elements, obtained from XRF analysis, are shown in Fig. 6a–c, Supp. Table S1. The Es_3^x shale samples are enriched

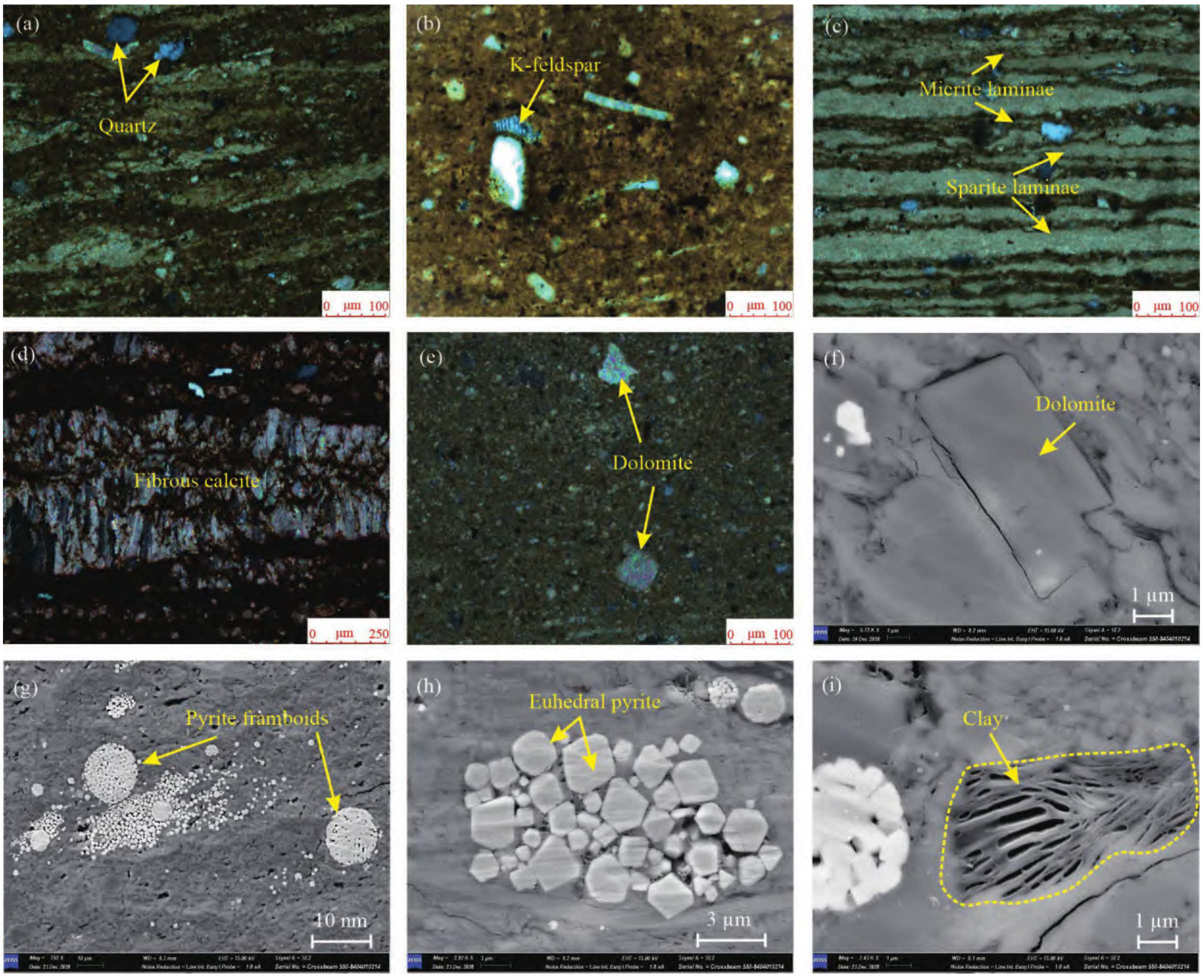

Fig. 3. Polarizing microscope photomicrographs, showing the characteristics of different minerals in the Es_3^x shale from well Luo-69.

(a) Quartz, 3045.3 m; (b) feldspar, 3013.2 m; (c) micrite and sparry calcite laminae, 3101.01 m; (d) fibrous calcite, 3058.25 m; (e) dolomite, 3024.1 m; (f) rhombohedral form of dolomite, 3045.3 m; (g) pyrite framboids, 2990.05 m; (h) distribution of euhedral pyrite, 3016.3 m; (i) characteristics of clay minerals, 3070.9 m.

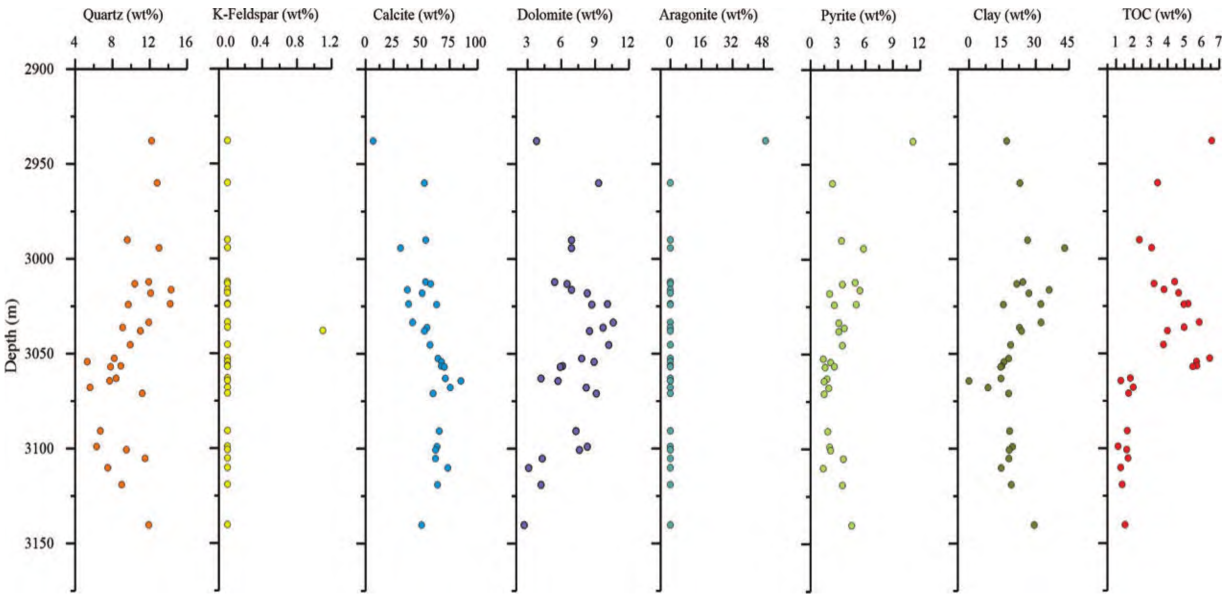

Fig. 4. The distribution and trend of various minerals and TOC contents, with respect to depth, in the study area.

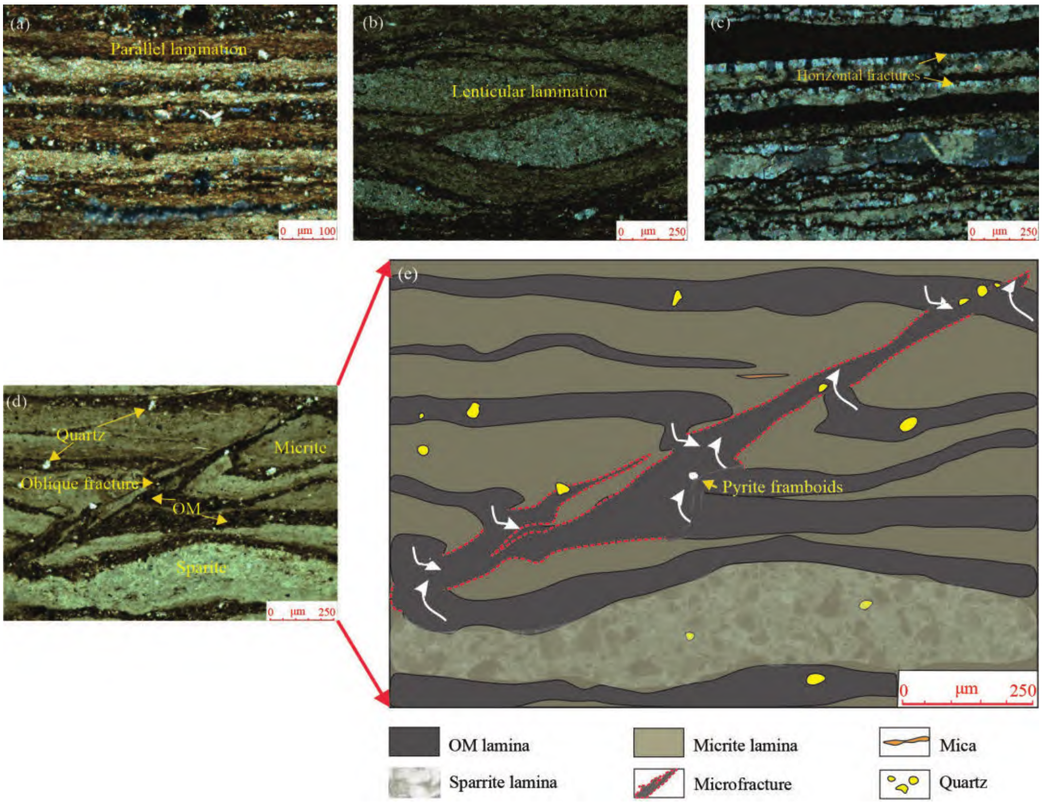

Fig. 5. Different types of syn-depositional and post-depositional sedimentary structures in the Es_3^x shale from well Luo-69.
(a) Parallel lamination, 3043.2 m; (b) lenticular lamination, 3054.3 m; (c) horizontal fractures filled with sparry calcite and OM, 3049.7 m; (d–e) oblique microfracture filled with OM and other minerals (clay and siliceous), 3116.7 m.

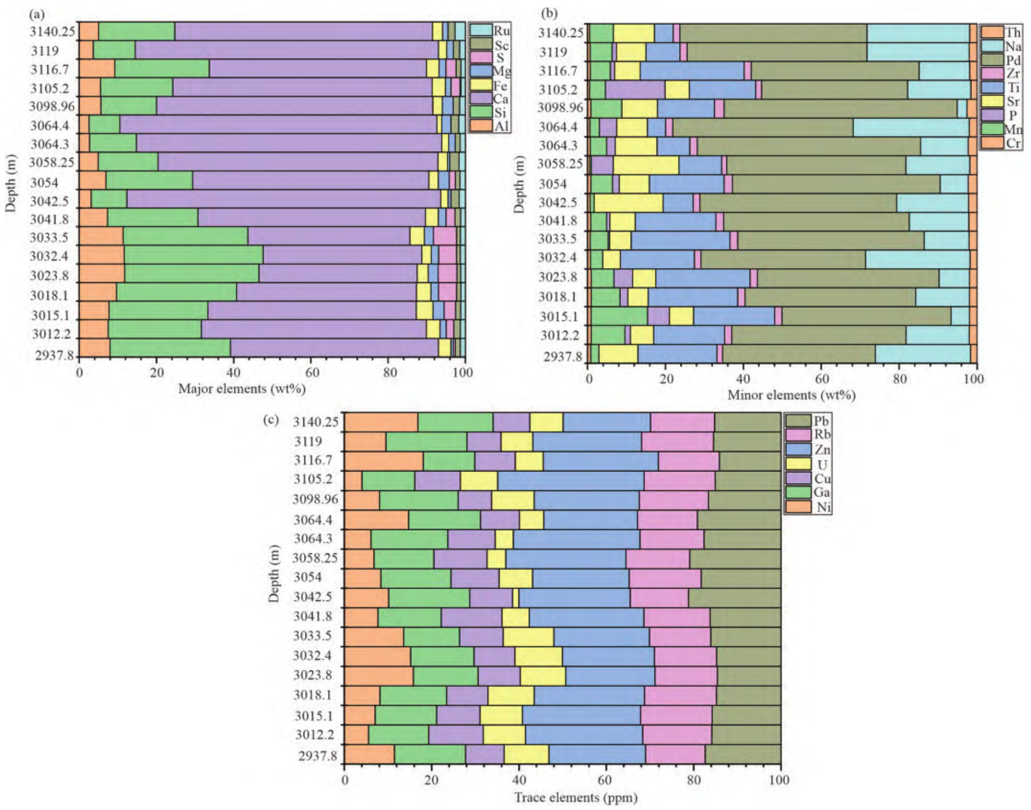

Fig. 6. Characteristics and distribution of (a) major elements, (b) minor elements and (c) trace elements in the Es_3^x shale.

with Ca (avg. 60.3 wt%), Si (avg. 21.3 wt%), Al (avg. 6.7 wt%), Fe (avg. 2.7 wt%), Mg (avg. 1.8 wt%), Sr (avg. 0.2 wt%), Ti (avg. 0.36 wt%), Mn (avg. 0.11 wt%), Zr (avg. 0.04 wt%), Rb (avg. 60.5 ppm) and some other elements (listed in Supp. Table S1). These elements are mainly associated with calcite, dolomite, quartz, clay minerals and pyrite. Numerous inorganic geochemical proxies were used to monitor the variations in various parameters of the depositional environment, including Rb/Sr, Ca/(Ca + Fe), Ti/Al, Al/Ti, Al/Ca and Zr/Rb. These ratios were used to predict the paleoclimate, salinity, detrital input, provenance and paleohydrodynamic conditions during the deposition of the Es_3^x shale. The details regarding the principles and usage of these elemental ratios are given in the discussion section.

4.5 Types of shale lithofacies

Currently, there is no uniformly accepted and standard classification system for the characterization of shale lithofacies. The classification system generally classifies diverse lithofacies in shale, based on mineralogy and TOC contents, coupled with sedimentary characteristics. Shale lithofacies have been established based on TOC contents, mineral composition, sedimentary structures and elemental geochemistry. Based on sedimentary structure, Es_3^x shale is composed of laminated shale (67.44%) and non-laminated shale (32.56%) (Fig. 7a). Based on TOC content, Es_3^x shale is comprised of organic-rich shale (50 wt%), organic-fair shale (16.67 wt%) and organic-poor shale (33.33 wt%) (Fig. 7b). After considering all types together, a total of six different types of shale lithofacies have been formalized, i.e., organic-rich laminated clay-bearing aragonitic shale (LF1), organic-rich non-laminated clay-bearing calcareous shale (LF2), organic-fair non-laminated calcite-bearing argillaceous shale (LF3), organic-rich laminated clay-bearing calcareous shale (LF4), organic-poor laminated clay-bearing calcareous shale (LF5) and organic-poor laminated quartz-bearing calcareous shale (LF6) (Fig. 7c). LF5 constitutes 34.88% of the total lithofacies in the Es_3^x shale, followed by LF2 (30.23%), LF4 (25.58%), LF6 (4.67%), LF1 (2.32%) and LF3 (2.32%) (Fig. 7d).

4.5.1 Organic-rich laminated clay-bearing aragonitic shale (LF1)

LF1 comprises nearly 49% aragonite, 17% clay, 12.2% quartz, 6.8% calcite, 11.2% pyrite and 3.8% dolomite. Calcite minerals appear in two different forms, namely micrite and sparite (Fig. 8a). LF1 possesses the highest amount of TOC contents (6.56 wt%) of all the lithofacies

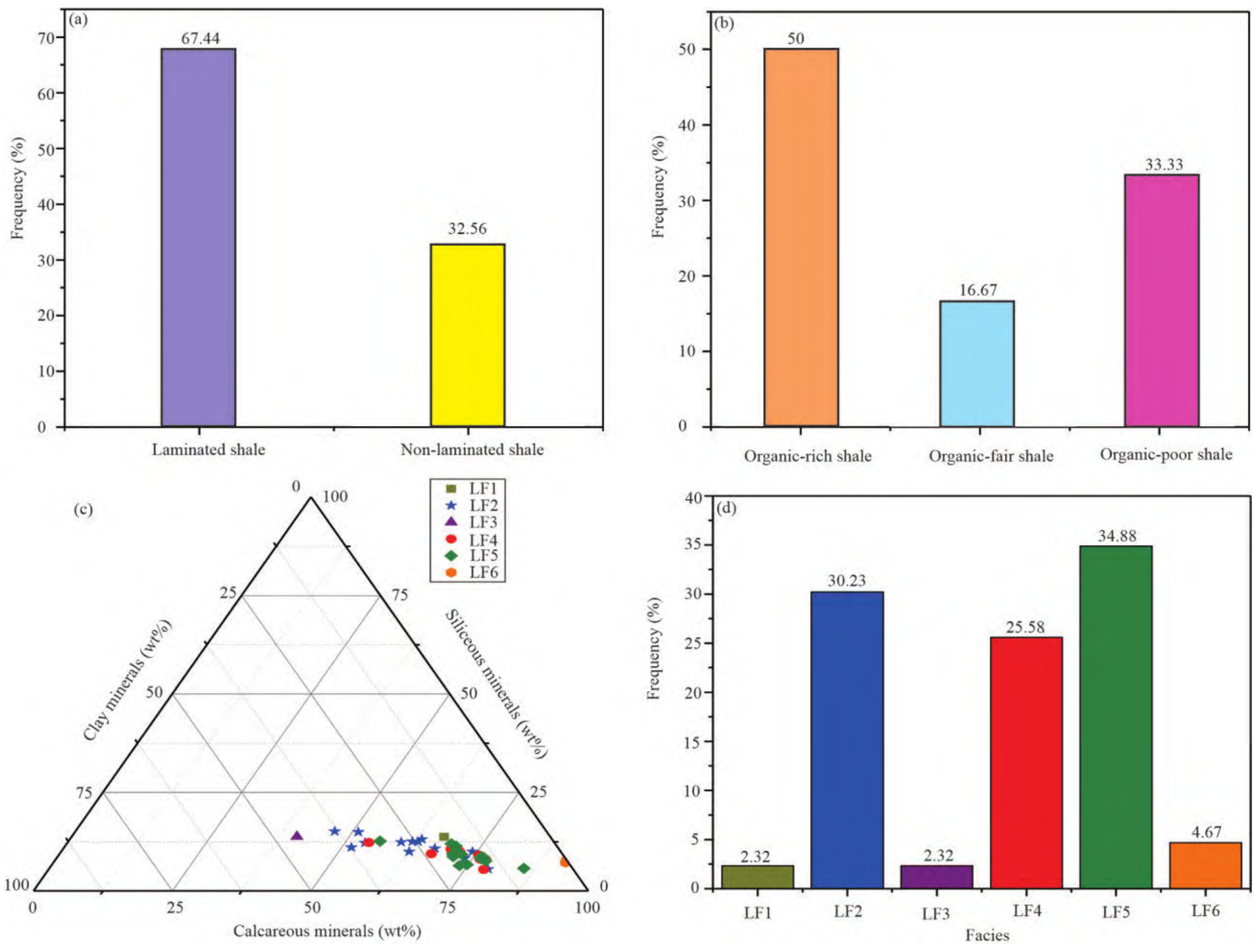

Fig. 7. Bar graphs and ternary diagram representing the characteristics of the Es_3^x shale in the Zhanhua Depression.
(a) Classifications of shale, based on sedimentary structures; (b) classifications of shale, based on TOC contents; (c) ternary diagram, representing the distribution of different types of shale lithofacies; (d) bar graph showing the frequency of lithofacies in the Es_3^x shale from well Luo-69.

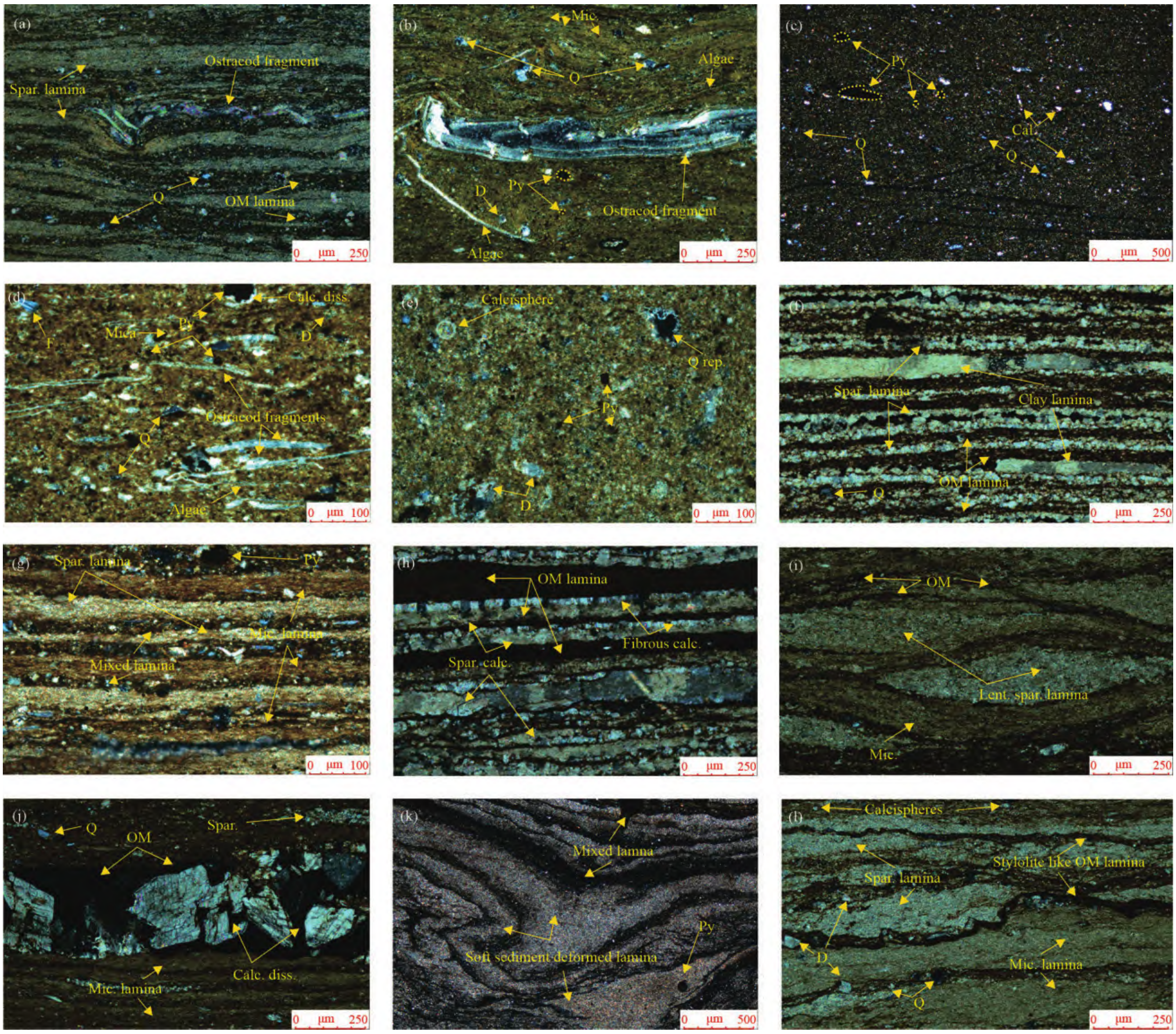

Fig. 8. Polarizing microscope photomicrographs, showing the characteristics of the Es_3^x shale lithofacies from well Luo-69.

(a) Sample of LF1, showing the sparite and OM lamina, along with ostracod fragment and quartz grains, 2937.8 m; (b) photomicrograph of LF1 lithofacies with some micrite content, algae, ostracod fragments, quartz, dolomite and pyrite grains, 2937.8 m; (c) sample of LF3 lithofacies, showing some calcite, quartz and pyrite grains, 2994.3 m; (d) photomicrograph of LF3 lithofacies, showing abundant biogenic contents, calcite dissolution, mica, feldspar, quartz, dolomite and pyrite grains, 3015.1 m; (e) sample of LF2 lithofacies, showing quartz replacement, pyrite, dolomite and calcisphere grains, 3024.1 m; (f–h) photomicrographs of LF4 lithofacies, showing the well-developed parallel lamination with various compositions, some sparite laminae, others are clay, OM, mixed, micrite and fibrous calcite laminae, 3042.5 m, 3043.2 m and 3049.7 m respectively; (i) sample of LF4, showing lenticular lamination with OM laminae, micrite laminae and sparite laminae, 3054.3 m; (j) photomicrograph of LF5, showing the dissolution and generation of crystalline calcite, 3067.8 m; (k–l) samples of LF5 and LF6 lithofacies, showing soft-sediment deformation and lenticular laminations, 3140.25 m and 3064.4 m, respectively.

Note: Cal. = calcite; Calc. diss. = calcite dissolution; Q. rep. = quartz replacement; Lent. Spar. = lenticular sparite; D = dolomite; Q = Quartz; Py = pyrite.

in the study area. The content of micritic calcite is higher than sparry calcite (recrystallized calcite containing isolated calcite grains). Pyrite framboids are observed in clay, silicate minerals and organic matter. Ostracod algal fragments and other microfossils are also observed (Fig. 8b). Lamination is present, but it is poorly developed in this lithofacies.

4.5.2 Organic-rich non-laminated clay-bearing calcareous shale (LF2)

LF2 has an average of 52.2% calcite, 10.7% quartz, 7.94% dolomite, 0.14% K-feldspar, 25.4% clay and nearly 3.5% pyrite. The TOC content ranges from 2.36–6.56 wt% with an average of 4.45 wt%. Micrite and sparry calcite are present. Recrystallized calcite (sparite) is also present along the edges of organic matter. A few quartz grains are coated by crystallized calcite (quartz replacement) (Fig. 8e). Pyrite is present in the form of pyrite framboids and is mostly encountered in clay and organic matter. A few biological components such as algae and other smaller fossils are also detected. Lamination is not developed in this lithofacies.

4.5.3 Organic-fair non-laminated calcite-bearing argillaceous shale (LF3)

LF3 is composed of nearly 31.3% calcite, about 13%

quartz, 6.9% dolomite, 43% clay, and 5.8% pyrite. Pyrite framboids are abundantly distributed throughout the clay and silicate minerals. This clay-dominated lithofacies has a few elongated quartz grains (Fig. 8c). It has nearly 3 wt% of TOC content. Lamination is not developed in this lithofacies.

4.5.4 Organic-rich laminated clay-bearing calcareous shale (LF4)

LF4 has an average mineralogical composition (based on XRD analysis) of about 60.2% calcite, nearly 9% quartz, 8.1% dolomite, 19.4% clay and 2.9% pyrite. This organic-rich shale has TOC content ranging from 3.76–5.83 wt% with an average content of 5.12 wt%. Lamination is partly lenticular and partly planar in some thin-sections (Fig. 8f–i). Light colored laminae are thicker than dark colored laminae. Light-colored laminae show micrite (in some sections sparite or fibrous calcite) while dark-colored laminae show organic matter, pyrite and clay minerals (mixed laminae) (Figs. 8f and 9g, h). Few isolated recrystallized sparite crystals, a few fibrous sparite laminae and a few organic clay laminae are also observed. Lamination is vividly developed in this lithofacies.

4.5.5 Organic-poor laminated clay-bearing calcareous shale (LF5)

LF5 has an average of 65.3% calcite, nearly 8.5% quartz, 5.8% dolomite, 17.7% clay and 2.4% pyrite. Organic-poor shale has a low TOC content (ranging from 1.12–2 wt% with an average of 1.5 wt%). Pyrite framboids are mostly encountered in clay and silicate minerals (Figs. 4e, 11g, i). In some sections, micritic calcite is abundant, while in others, sparite concentration is very high. Lamination is lenticular in so.me parts, while laminations having soft-sediment deformation are present in other areas of the thin-sections (Fig. 8j, k). Light colored laminae are thicker than dark colored laminae. Dissolution and recrystallization of sparite are common in some areas (Fig. 8j).

4.5.6 Organic-poor laminated quartz-bearing calcareous shale (LF6)

LF6 has an average mineralogical composition of 84.5% calcite, nearly 7.3% quartz, 5.6% dolomite, 0.25% clay and 2.2% pyrite. Framboidal pyrite is encountered during petrography, being commonly present in organic matter and clay-quartz mixed laminae. Organic-poor shale has 1.2 wt% of TOC content. Micritic calcite is more abundant than sparry calcite (Fig. 8l). Lamination is partly lenticular and partly planar. Light colored laminae are thicker than dark colored laminae.

5 Discussion

5.1 Interpretation of depositional environment based on geochemical analysis

Elemental geochemistry (major, minor and trace elements) is extensively used to describe the characteristics of various parameters of depositional environments, including paleoclimate, paleo-salinity, detrital influx, paleohydrodynamic conditions and provenance (Koh et al., 2016; Odabasi et al., 2016). The analysis of the main constituents of elemental geochemistry ratifies the stratigraphic characteristics shown in Table 2, while the evolution of the sedimentary setting in the study area is presented in Fig. 9. In this study, various geochemical proxies were utilized to interpret the depositional environment, including Rb/Sr, Ca/(Ca + Fe), Ti/Al, Al/Ca, Al/Ti and Zr/Rb. The sedimentary environment is analytically evaluated in terms of paleoclimate, paleosalinity, detrital influx, paleohydrodynamic conditions and provenance (Table 2).

Rb/Sr ratios are used for paleoclimate analysis and here they range from 0.013 to 0.054 with an average of 0.037, generally <0.5 (Zhang et al., 2013; Fig. 9). The result deduced from these ratios suggests that the sedimentary environment of the Es_3^x shale was humid. According to Xu et al. (2015), Rb/Sr ratios greater than 0.03 indicate warm humid conditions, the average ratio of Rb/Sr in the study area being 0.037. Therefore, it indicates warm humid climatic conditions at the time of deposition. Due to higher calcium content, the ratios of Ca/(Ca + Fe) were high, ranging from 0.92 to 0.99 (avg. 0.96). These values show that the water was saline during the deposition of the Es_3^x shale (Zhang et al., 2013). Ti/Al ratios range from

Table 2 Elemental geochemical analysis of the Es_3^x shale in the Zhanhua Depression

Depth	Paleoclimate	Salinity	Detrital influx	Provenance		Paleohydrodynamic conditions
(m)	Rb/Sr	Ca/(Ca + Fe)	Ti/Al	Al/Ca	Al/Ti	Zr/Rb
2937.8	0.022	0.943	0.065	0.147	15.27	6.535
3012.2	0.048	0.942	0.054	0.128	18.19	6.288
3015.1	0.047	0.926	0.057	0.142	17.42	6.253
3018.1	0.053	0.925	0.049	0.207	20.14	6.745
3023.8	0.044	0.934	0.042	0.286	23.74	7.189
3032.4	0.053	0.943	0.039	0.283	25.01	7.135
3033.5	0.051	0.918	0.044	0.270	22.42	7.067
3041.8	0.045	0.946	0.054	0.124	18.32	6.800
3042.5	0.012	0.976	0.061	0.037	16.19	7.568
3054	0.040	0.961	0.057	0.112	17.28	6.866
3058.25	0.013	0.966	0.063	0.067	15.68	5.923
3064.3	0.023	0.977	0.062	0.033	16.036	7.648
3064.4	0.027	0.984	0.053	0.030	18.63	8.296
3098.96	0.036	0.966	0.050	0.078	19.80	7.385
3105.2	0.039	0.950	0.077	0.081	12.82	6.204
3116.7	0.042	0.945	0.062	0.163	16.06	6.495
3119	0.032	0.973	0.060	0.046	16.59	7.354
3140.25	0.021	0.962	0.042	0.074	23.59	7.391

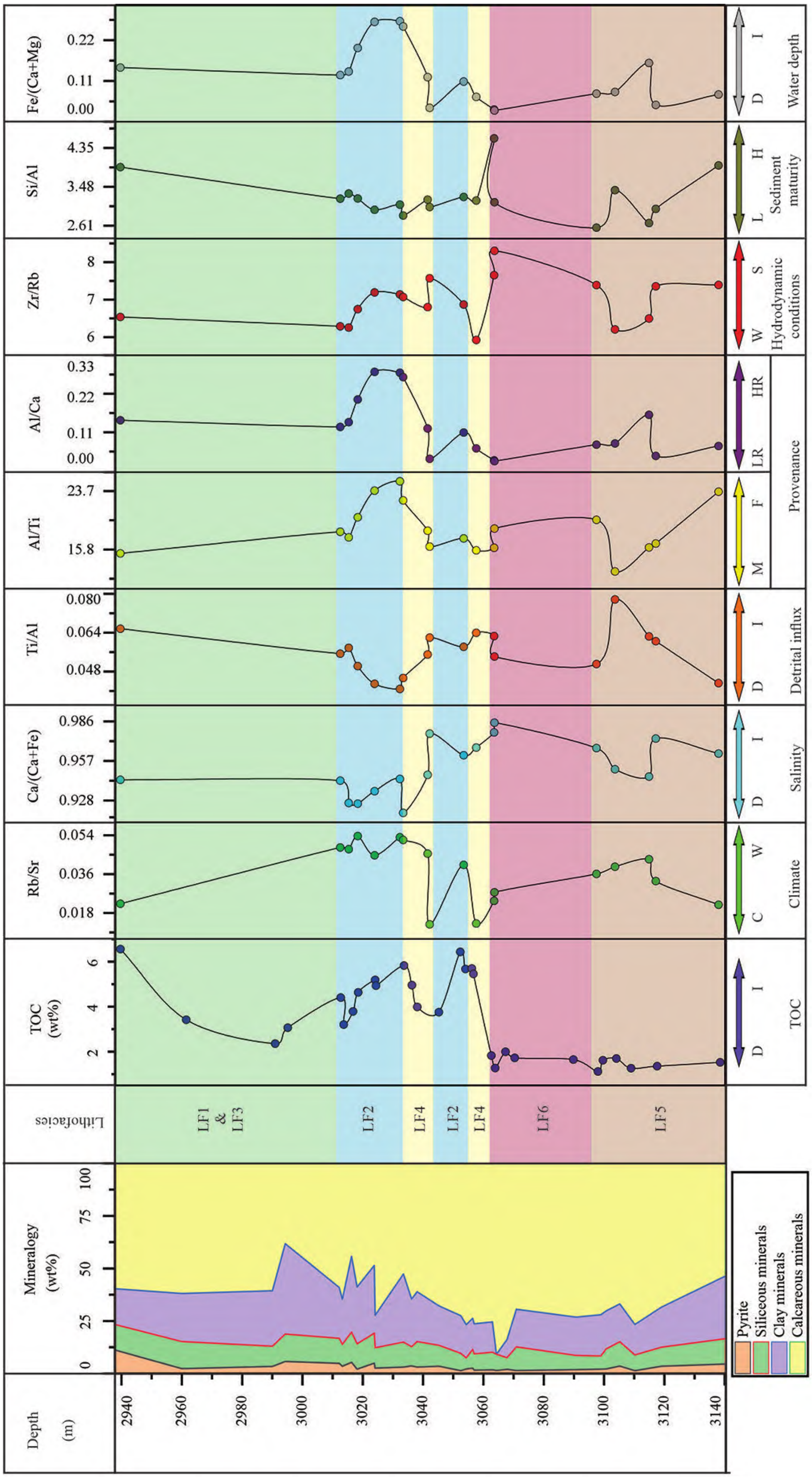

Fig. 9. Geochemical proxies for analysis of the paleodepositional environment of Es_3^x shale from well Luo-69.

Note: For TOC, salinity, detrital influx and water depth, D = decrease and I = increase, climate (C = cold and W = warm), provenance (Al/Ti) (M = mafic and F = felsic), provenance (Al/Ca) (LR = low sedimentation rate and HR = high sedimentation rate), hydrodynamic conditions (W = weak and S = strong).

0.039 to 0.077 (avg. 0.055) and this average value indicates the restricted detrital influx during deposition (He et al., 2017). Al/Ca ratios range from 0.03 to 0.29 with an average value of 0.14. These ratios generally show that the sedimentation rate from the provenance area was lower during the early phase of deposition than in the later phase (Picard, 1971; Cao et al., 2007; Yang et al., 2015). Subsequently, the sedimentation rate from the provenance was relatively low, but increased with decreasing water depth (Fig. 9).

Al/Ti ratios are also used to interpret the provenance, as their values are close to the parent rocks (Moradi et al., 2016). As such, the ratios of Al/Ti range between 8 to 21, the binary plot of Ti versus Al of the studied samples suggest the dominance of intermediate igneous rocks in the source area (Fig. 10). Zr/Rb ratios in the studied sections vary from 5.93 to 8.3, with an average value of 6.96. The average value of Zr/Rb in the study area is 6.96, which is greater than 6.02, indicating higher hydrodynamic conditions (Tenger et al., 2006). The trend slightly decreases from bottom to top, which means that the hydrodynamic conditions were higher during the earlier phase of deposition than the later.

5.2 Interpretation of depositional environment based on mineral composition

The depositional environment can also be reconstructed based on mineral abundances (Table 1). Dry climatic conditions with higher evaporation are favorable for the precipitation of calcareous minerals. A cleaner and enclosed water body with a lack of terrigenous influx also provides favorable conditions for the deposition of calcareous minerals (Scholle et al., 1983; Zhu et al., 2005). The calcareous minerals are mostly authigenic in the study area (Zhu et al., 2005) and they show a negative correlation with silicate and clay minerals (Fig. 15). Therefore, their bulk precipitation and concentration show the presence of highly saline and cleaner water under warm climatic conditions (Tonger, 2004; Yu et al., 2014; Yang et al., 2015). Silicate and clay minerals are predominantly terrigenous in the Es_3^x shale, hence, their low contents represent the low terrigenous input from terrestrial sources (Bomou et al., 2013; Montero-Serrano et al., 2015). Pyrite can be used to observe the paleoredox conditions of the prevailing water body, due to its formation in more reducing sedimentary environments (Yang et al., 2015; Khan et al., 2021). Pyrite is mostly observed in the form of pyrite framboids under the polarizing microscope and FE-SEM analysis (Fig. 11a–f). It ranges from 1.3% to 11.2% with an average of 3.3% (Table 1). Hence, it can be deduced that during the deposition of Es_3^x shale, strong reducing conditions prevailed. The chemistry of the prevailing water body can be inferred from the size of the pyrite framboids, because it is associated with the chemical conditions of the ancient water body in which they precipitated (Wilkin et al., 1996; Loucks and Ruppel, 2007; Khan et al., 2021). The positive relationship of pyrite with TOC and TS (total sulfur) shows that pyrite is formed under reducing conditions (Fig. 12a). Pyrite framboids in the Es_3^x shale are predominantly present in small sizes (Fig. 11), therefore we can suggest that they were precipitated from a euxinic water body (anoxic plus sulfidic) (Khan et al., 2021).

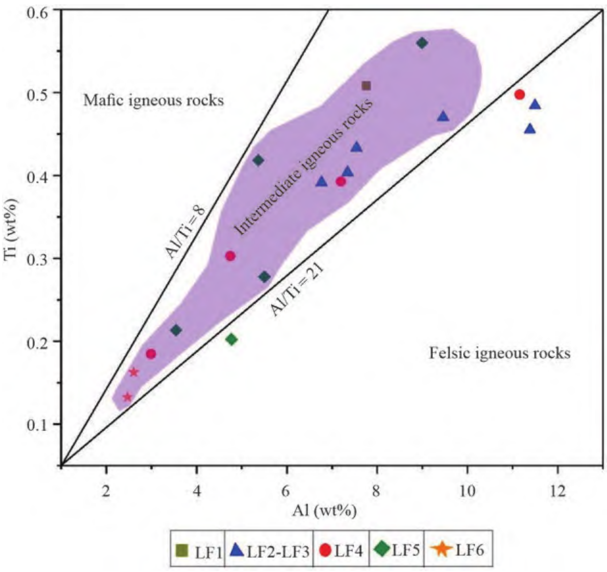

Fig. 10. Ti versus Al diagram for provenance analysis of the Es_3^x Shale. Al/Ti ratios between 8 and 21 show that the provenance of Es_3^x shale is intermediate igneous rock. Only a few samples show a felsic igneous rock provenance (modified after Moradi et al., 2016).

5.3 Analysis of depositional environment based on TOC content

The characteristics of the depositional environment can also be described based on the presence of organic matter in the shale. In the Es_3^x shale, the plentiful TOC content (Table 1) shows the dominance of a reducing sedimentary environment where bacterial degradational action is absent that destroys the organic matter and its preservation potential (Loucks and Ruppel, 2007). Bacterial interaction would have destroyed and dispersed much of the organic matter if the bottom conditions of the water body had been aerobic, because bacteria can use most organic components as nutrients. The paleoredox conditions of a water body can also be identified by using a relationship between TOC and TS (Rimmer et al., 2004). A TOC/TS ratio of less than 1.5 shows anoxic conditions, between 1.5–5 shows suboxic, and greater than 5 shows oxic water conditions (Fig. 12c). Mn/TS and TS/Fe ratios were also used to predict the paleoredox conditions of the water body during deposition (Mansour et al., 2020). The lowest values of Mn/TS reflect the anoxic environments, while a higher TS/Fe ratio (also indicates the zone of excess sulfur) shows a more reducing environment during deposition of the Es_3^x shale (Fig. 12d). The highest values of TS/Fe from 1 to >1 show the zone of excess sulfur (euxinic conditions) in the study area (Fig. 12d).

5.4 Analysis of depositional environment based on sedimentary structures

Sedimentary structures are also a good source of information with which to describe the characteristics of depositional environments. Laminations are one of the important sedimentary structures that are commonly developed in shale and other fine-grained rocks. Euxinicity of a water body can be inferred based on laminations and the absence of benthic fauna (Berner, 1984), the presence of laminations and a lack of benthic fauna in the Es_3^x shale showing evidence of euxinic depositional conditions. During petrographic analysis, it was revealed that laminations start appearing with

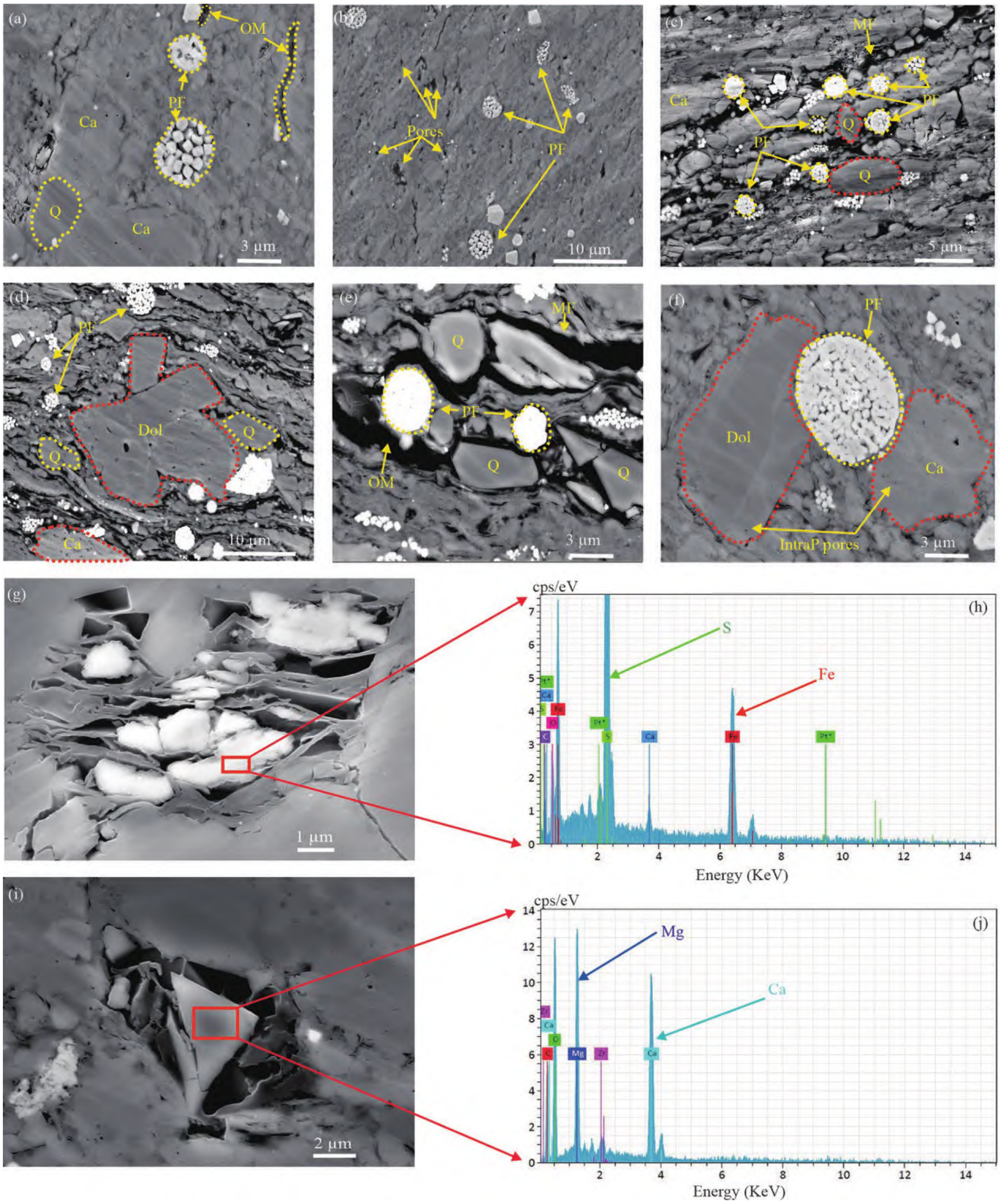

Fig. 11. FE-SEM photomicrographs, representing the mineralogical characteristics of the Es_3^x shale.
(a–c) Sample of LF2, showing the distribution of pyrite framboids, OM, calcite, dolomite, quartz, MF and some pores, 3012.2 m (a–b) and 3023.8 m (c); (d–f) samples of LF4, representing the intraparticle pores, PF, MF, quartz, OM, calcite and dolomite, 3033.5 m (d–e) and 3045.3 m (f); (g, i) SEM photomicrographs with EDS spectrum, showing the elemental composition of minerals in the selected area, 3064.3 m and 3098.96 m, respectively; (h) EDS of Fig. 11g shows pyrite grains while (j) Fig. 11i shows dolomite.
Note: Ca = calcite; Q = quartz; PF = pyrite framboids; MF = microfracture; Dol = dolomite; IntraP = intraparticle.

increasing burial depth. Non-laminated shale shows no variation in sedimentary environments that cause differences in layers also showing stagnant water bodies and slow deposition (Fig. 8d). The laminated shale samples show different types of laminated layers, such as parallel and lenticular laminations (Fig. 8f, k, l). Parallel laminations are formed by short-lived, or less severe, fluctuations in sedimentary depositional conditions than those that produce beds. They have resulted from fluctuating depositional environments that create variations in grain size, contents of clay, organic material, mineralogy and/or micro-palaeontological contents (Boggs, 2006). Lenticular laminations are formed where fluctuations in sediment influx and current velocity commonly prevailed (Nichols, 2009). They display consistent variations in hydrodynamic conditions in various parts of the Es_3^x shale (Fig. 9). Laminations have the greatest potential for preservation in reducing or anaerobic depositional settings, where the organic activity is minimal, or in environments where the sedimentation rate is so rapid that the sediment is buried below the depth of an active organic reworking before organisms can obliterate the lamination (Berner, 1984; Boggs, 2006). Therefore, the presence of laminations can also show the reducibility of the depositional environment during the deposition. On the other hand, the lack of bioturbation and, ultimately, the absence of micro-organisms, also confirms the reducing depositional conditions during the deposition of the Es_3^x shale.

5.5 Effect of depositional environment on the evolution of shale lithofacies

Warm and humid climatic conditions with low salinity are favorable for biogenic richness, along with adequate nutrients being supplied by terrigenous influx for their development (Fig. 13a; Gautier, 1986). The preservation potential of organic matter (OM) is significantly boosted by the abundance and distribution of biogenic contents, because these contents can produce a bulk quantity of OM that consumes the oxygen supply, thus preserving the OM (Curtis, 2002). Freshwater inflow reduces the salinity and makes this sedimentary environment favorable for high

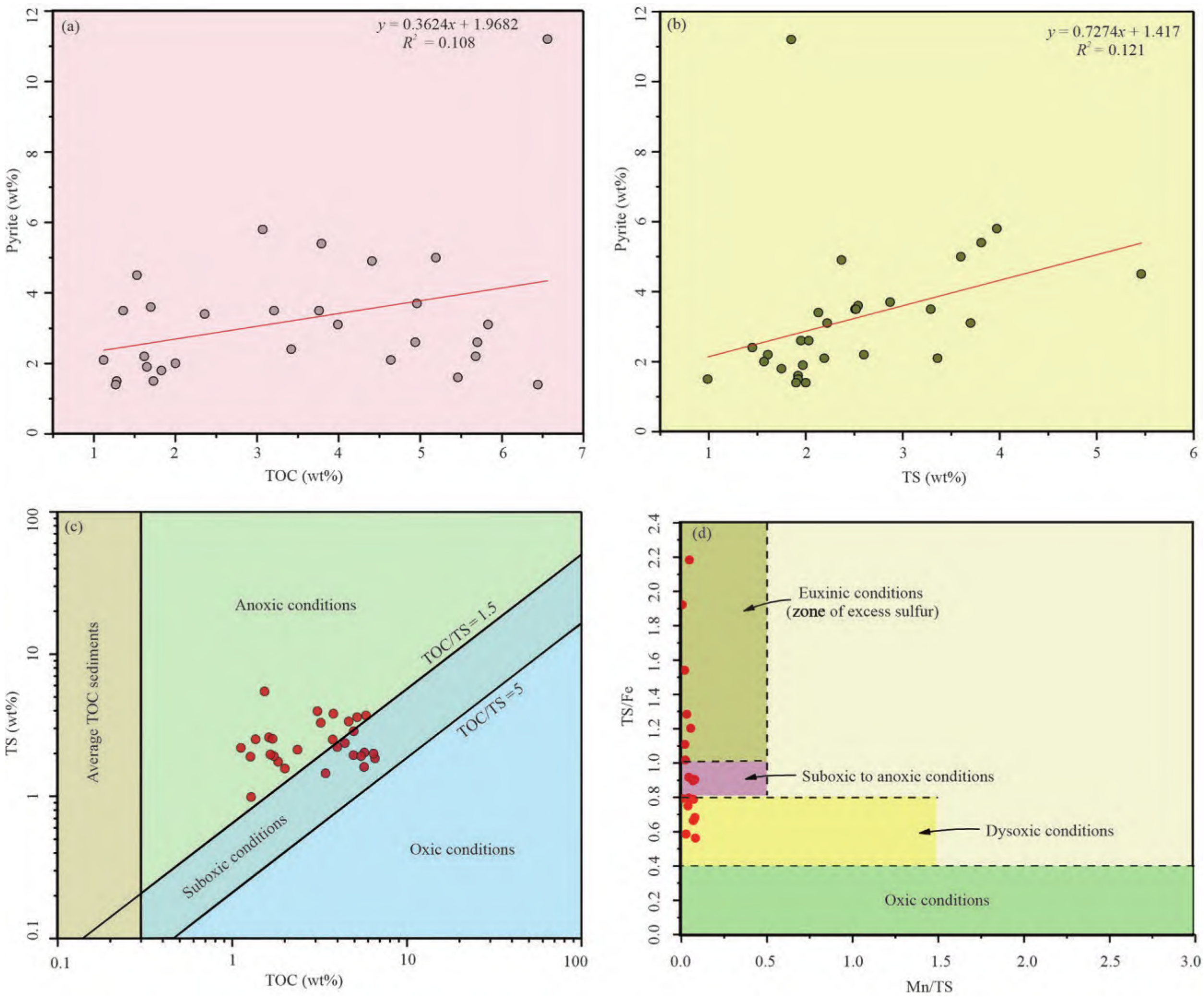

Fig. 12. Interpretation of paleoredox conditions.
(a) Positive relationship between TOC and pyrite; (b) positive relationship between TS and pyrite; (c) plot between TOC and TS; (d) variation between Mn/TS ratio and TS/Fe ratio, showing redox conditions during deposition of the Es_3^x shale (modified after Mansour et al., 2020).

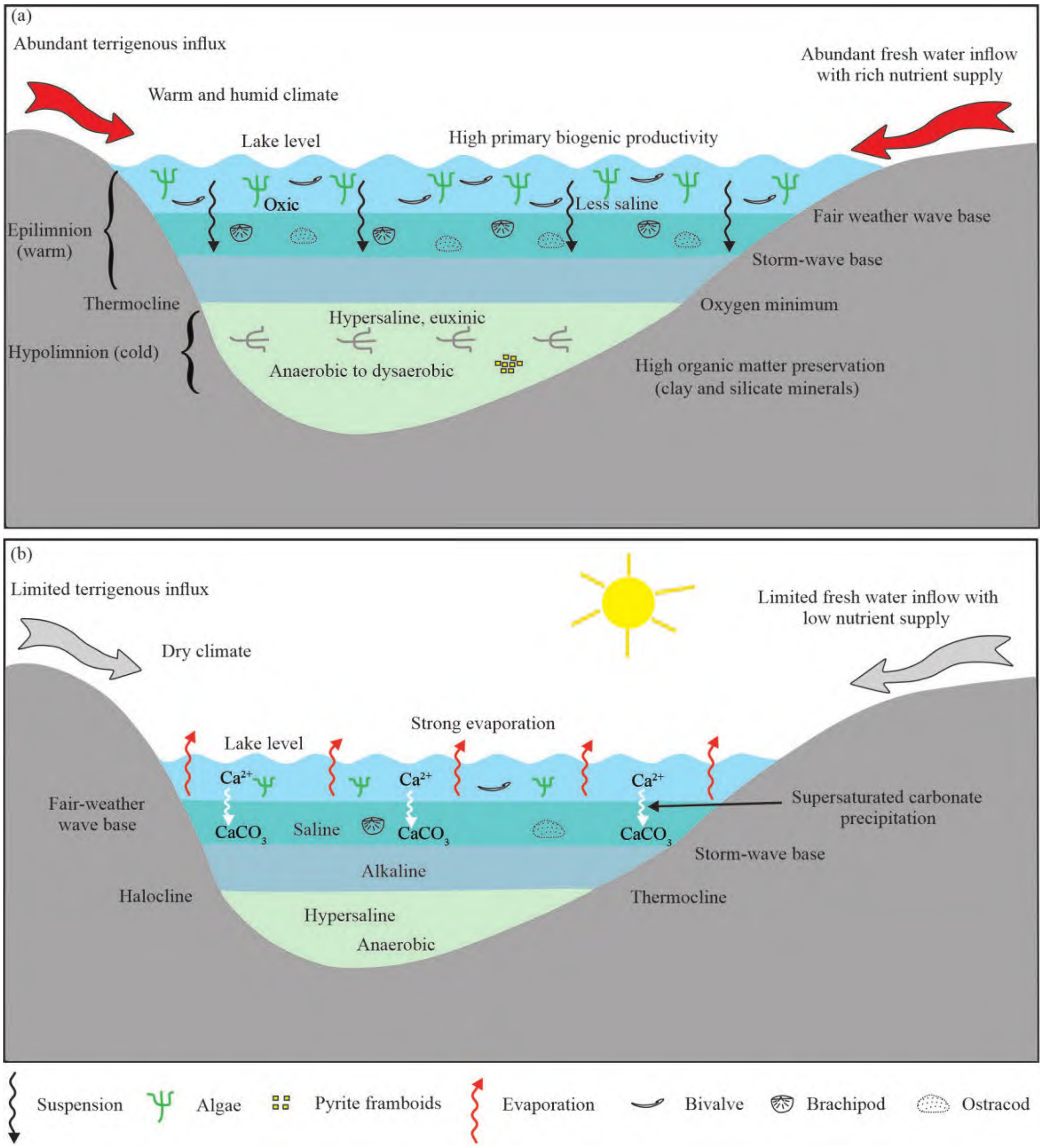

Fig. 13. Detailed sedimentary model showing variations in different environmental factors during the deposition of the Es_3^x shale.
(a) Model showing the humid climatic conditions with sufficient terrigenous influx and freshwater flow; (b) model showing the dry climate with limited terrigenous input and strong evaporation.

Table 3 Characteristics of the sedimentary depositional environment for different types of observed lithofacies in the Zhanhua Depression

Geochemical proxies and mineral composition		Lithofacies					
		LF1	LF2	LF3	LF4	LF5	LF6
Paleoclimate	Rb/Sr	0.02	0.04	0.04	0.03	0.03	0.025
Salinity	Ca/(Ca+Fe)	0.94	0.94	0.8	0.95	0.95	0.98
Detrital influx	Ti/Al	0.06	0.04	0.05	0.05	0.05	0.05
Provenance	Al/Ti	15.3	20.51	20.52	18.45	17.90	17.33
	Al/Ca	0.14	0.19	0.18	0.13	0.09	0.032
Paleohydrodynamic conditions	Zr/Rb	6.53	6.74	6.67	6.80	6.91	7.97
Sediment maturity	Si/Al	3.91	3.16	3.2	3.04	3.15	3.84
Water depth	Fe/Ca+Mg	0.14	0.18	0.19	0.12	0.09	0.031
TOC	(wt%)	6.56	4.45	3.07	5.12	1.57	1.28
Calcareous minerals	(%)	59.6	60.20	38.2	68.46	71.09	90.8
Siliceous minerals	(%)	12.2	10.84	13	9.05	8.56	7.7
Clay minerals	(%)	17	25.44	43	19.43	17.71	0.5

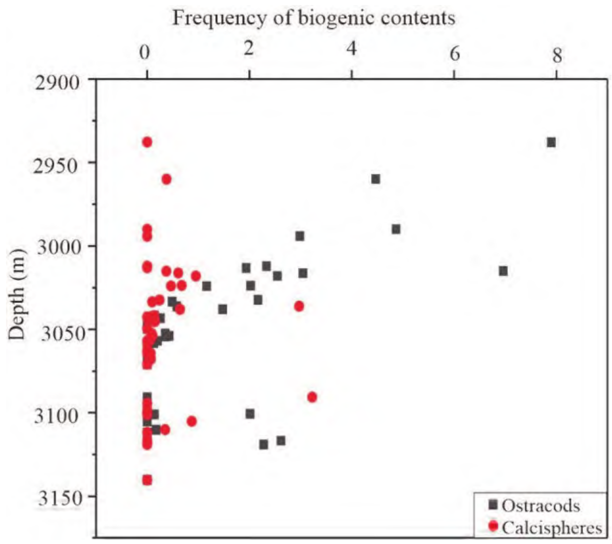

Fig. 14. Distribution of various biogenic contents (ostracods and calcispheres) in the Es_3^x shale. The frequency of biogenic contents is decreasing with increasing burial depth, showing that during the earlier phase of deposition, primary biogenic productivity was high.

biogenic productivity (Figs. 13a and 14). The sedimentary environment during the deposition of LF6 was highly reducible and had the lowest TOC contents (Table 3). This phenomenon took place due to dry climatic conditions, higher salinity and the lowest provenance (Table 3). These pieces of evidence indicate that the climate, salinity and provenance all play important roles in the accumulation of OM. The strongly-reducing depositional environment provides good preservation conditions for the accumulation of abundant OM. Quartz and clay minerals are transported as a terrigenous influx, therefore, they have a weak positive relationship with TOC contents (Fig. 16a–b).

Evaporation is caused by warm and drier environmental conditions and these conditions support the precipitation of calcareous minerals (Fig. 13b). A restricted water body, having a very limited terrigenous influx, also provides favorable depositional conditions for calcareous minerals (Fig. 14b, Scholle et al., 1983; Zhu et al., 2005). Calcareous minerals have a strong negative relationship with clay, quartz and pyrite, due to these prevailing conditions (Fig. 15). Highly salinized sedimentary environments are always conducive to the deposition of calcareous minerals, which is detrimental to the development of biogenic contents (e.g., fish and algae), but it is ideal for the proliferation of anoxic bacterial

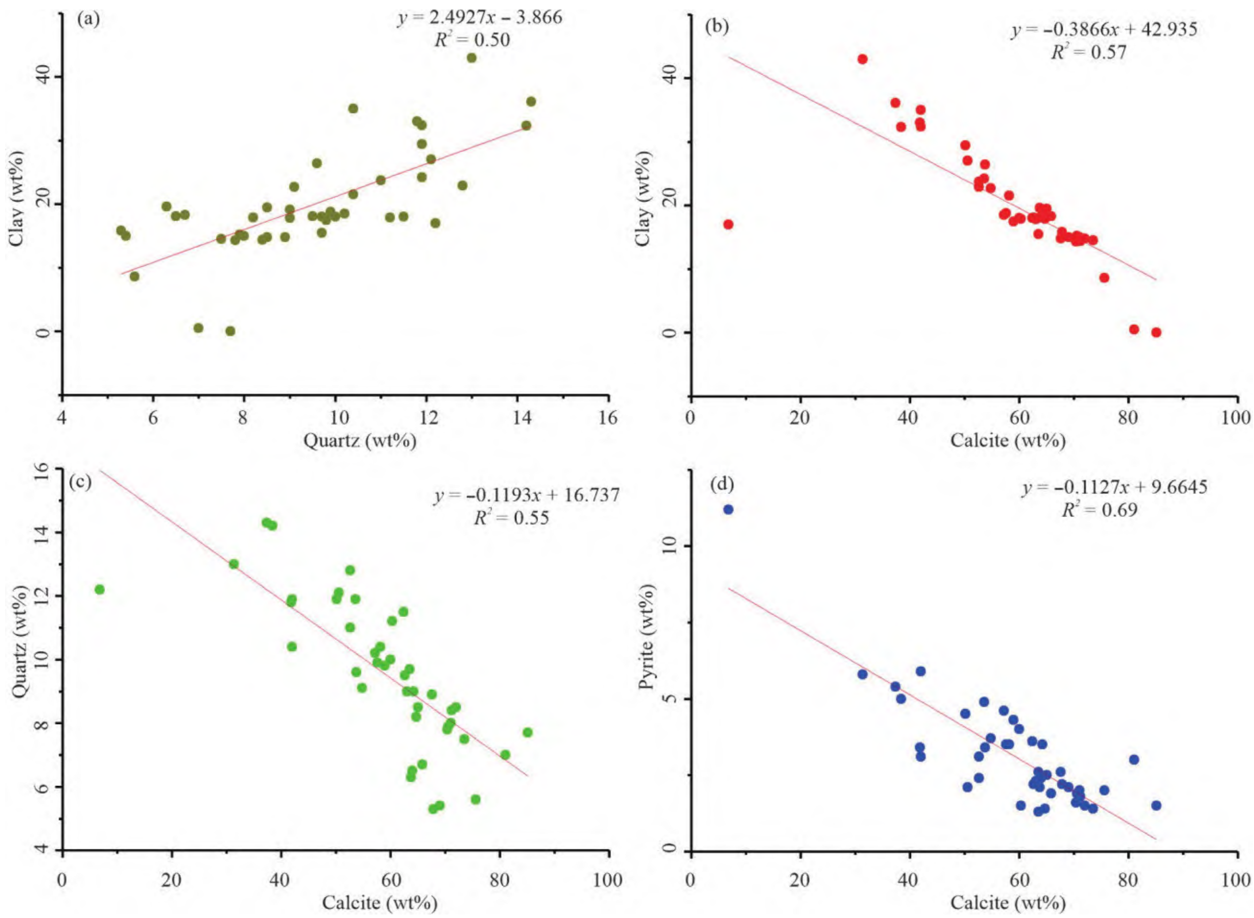

Fig. 15. (a–d) Showing the linear relationships between different minerals.
This relationship between the different types of minerals largely depends on the prevailing sedimentary environment at the time of deposition.

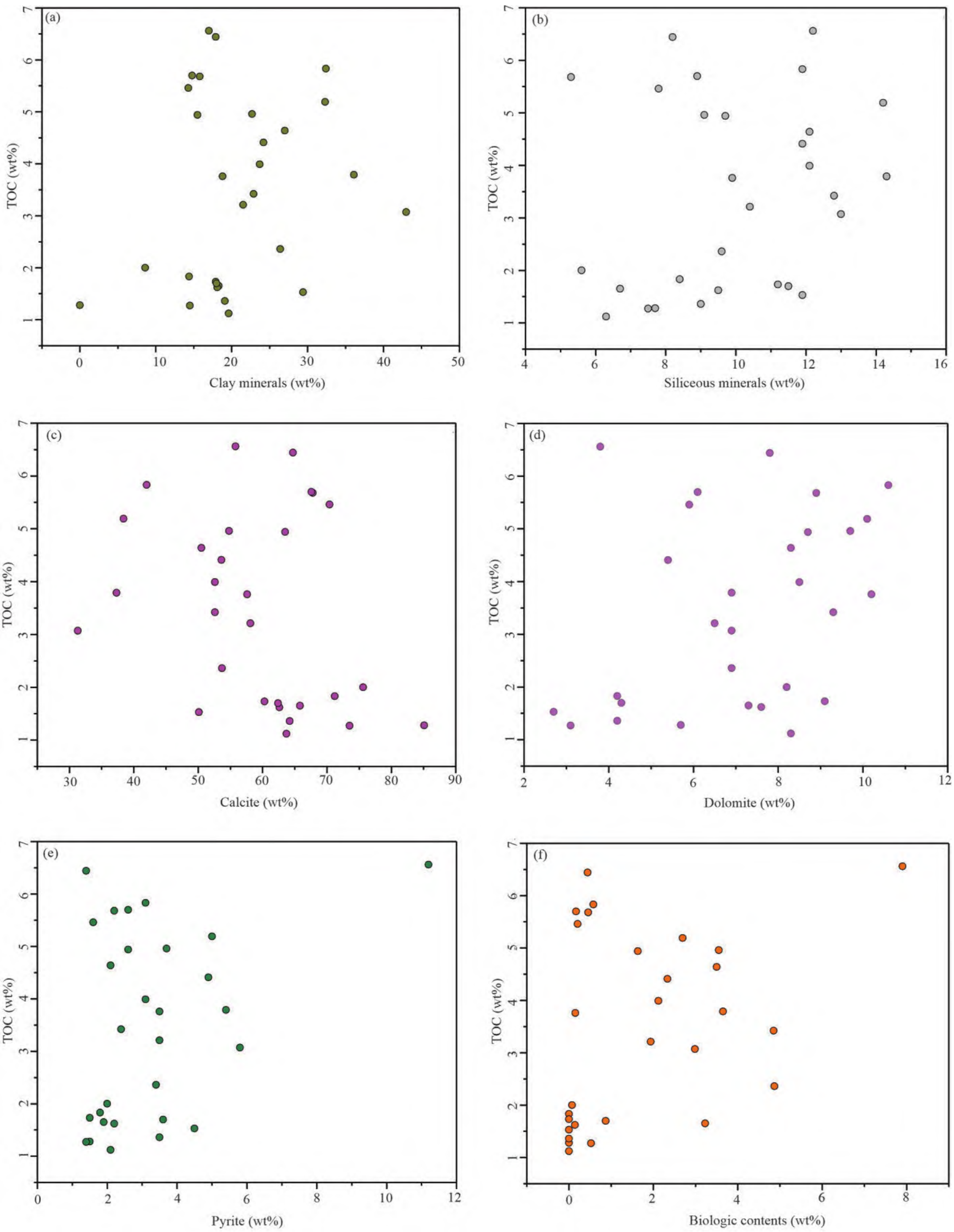

Fig. 16. The correlation of TOC content with different minerals shows a positive and negative linear relationship.
(a–b) Clay and silicate minerals have a positive (weak) linear relationship with TOC content; (c) calcite has a negative (weak) linear relationship with TOC content; (d) dolomite has a positive relationship with TOC content; (e) pyrite has a strong positive relationship with TOC content; (f) biological contents also show a strong positive correlation with TOC content.

content (Murphy and Wilkinson, 1980). Calcareous minerals (especially calcite minerals) have a negative correlation with TOC content because when the concentration of carbonate material increases, then it leads to the reduction of TOC during deposition, due to the dilution effect of the carbonate influx (Ricken, 1996; Fig. 16c). But dolomite has a positive relationship with TOC because authigenic dolomite in the Es_3^x shale is microbially-mediated dolomite (Fig. 16d; Li et al., 2020). Previous research (Vasconcelos and McKenzie, 1997; Warren, 2000), has indicated that OM associated with the mediation of microbial organisms encourages the formation of dolomite. Due to the driest climatic conditions, the lowest provenance and the highest salinity, LF6 displays the maximum level of calcareous minerals (average of 90.8%) (Table 3).

LF1 has a high detrital influx, higher provenance, low paleohydrodynamic conditions and high biogenic content (Fig. 14; Table 3). Due to these prevailing conditions, LF1 has high clay and silicate mineral contents, intermediate calcareous content and higher pyrite content than other lithofacies (Table 3). The higher pyrite contents indicate that the depositional environment was highly reducible, which supports the preservation of OM. Therefore, this lithofacies has the highest amount of TOC content, TOC having a strong positive relationship with pyrite and biological contents (Fig. 16e, f; Table 3). The types of laminations (light-colored and dark-colored) that are formed in LF1, LF4 and LF6 lithofacies are closely linked to the layers of the water body, which could result in seasonal internal and external sediments (Loucks and Ruppel, 2007). The stratification in the water body is triggered by variations in salinity and temperature (Glenn and Kelts, 1986). LF2 is marked by higher salinity, high provenance and high TOC content. Warm and humid climatic conditions prevailed during the deposition of this lithofacies (Table 3). Large contents of clay minerals also confirm the higher provenance in this lithofacies. The TOC content and clay minerals have a positive relationship in this lithofacies, which also suggests that clay minerals played an important role in the distribution of organic matter during the deposition of LF2 (Fig. 16a).

During the summer season, the water body temperature increases, due to the stronger effect of sunlight. In these conditions, algae relentlessly extract carbon dioxide from the water through the photosynthetic process, leading to the precipitation and enrichment of calcareous mineral contents and the consequent development of light-colored laminations. During the winter season, the temperature of the water body decreases significantly and planktonic foraminifera and algae die. Due to lower temperatures, the water body circulation weakens and the bottom of the water body becomes anoxic and quiet. Clay minerals, silicate minerals and the organic material that are all suspended at the surface of the water body start settling down and form dark-colored thin laminations (Fig. 13a, b; Lallier-Verges et al., 1996; Dean, 1999). A euxinic water body at the bottom played a significant role in the development and preservation of laminations in the laminated lithofacies of the Es_3^x shale, as if there had been oxic conditions, then the laminated layers would have been demolished, due to extensive bioturbation (Loucks and Ruppel, 2007).

The results deduced from detailed observations of the Es_3^x shale in the Zhanhua Depression indicate that the mineralogy, TOC content and sedimentary structures of the shale are controlled by various parameters of the depositional environment, including climate, salinity, detrital influx, provenance, paleohydrodynamic conditions and paleoredox conditions. The sedimentary settings during the deposition of the Es_3^x shale had warm and humid climatic conditions, higher salinities, restricted detrital influx, intermediate igneous provenance, high paleohydrodynamic conditions and strongly reducing conditions. As a result of these factors, the Es_3^x shale is characterized by higher calcite content, moderate clay minerals and lower siliceous minerals, with higher TOC content and extensive laminations.

6 Conclusions

The results show that the Es_3^x shale is composed of calcite (avg. 58.5%), dolomite (avg. 7%), quartz (avg. 9.6%), clay minerals (avg. 20%) and pyrite (avg. 3.2%). It is characterized by high TOC content (average of 3.49 wt%). Two common types of sedimentary structures are observed in the Es_3^x shale, including syn-depositional structures (parallel and lenticular laminations) and post-depositional structures (microfractures). Six different types of shale lithofacies—LF1, LF2, LF3, LF4, LF5 and LF6—have been established based on mineralogical composition, TOC contents and sedimentary structures. These lithofacies are controlled by different parameters of the depositional environment in the basin. The depositional environment of the Es_3^x shale is divided into two phases; the earlier phase is marked by a dry climate, higher salinity, abundant detrital influx and strongly reducing conditions. The sedimentary environment during the later phase of deposition had warm and humid climatic conditions, higher salinities, limited detrital influx, high paleohydrodynamic conditions, higher reducibility and intermediate igneous rock provenance. The characteristics of the depositional setting greatly affect the mineralogical composition, TOC contents and sedimentary structures, which correspond to the evolution of the Es_3^x shale lithofacies in the study area.

Acknowledgments

This research work was supported by the National Science and Technology Major Project of China (Grant No. 2017ZX05009-002), the National Natural Science Foundation of China (Nos. U1762217, 41702139, 42072164 and 41821002), Taishan Scholars Program (No. TSQN201812030) and the Fundamental Research Funds for the Central Universities (19CX07003A). The authors would also like to acknowledge the School of Geosciences, China University of Petroleum, East China, for analytical support and financial support. This manuscript greatly benefited from the constructive comments and prolific suggestions of the two anonymous reviewers. We also thank Dr. Hou Zengqian and Dr. Fei Hongcai for editorial handling of the manuscript.

Manuscript received Feb. 17, 2022
accepted Aug. 8, 2022
associate EIC: ZHANG Shuichang
edited by Jeffery J. LISTON and FEI Hongcai

Supplementary material to this article can be found online at https://doi.org/10.1111/1755-6724.14985.

References

Abouelresh, M.O., and Slatt, R.M., 2012. Lithofacies and sequence stratigraphy of the Barnett Shale in east-central Fort Worth Basin, Texas. AAPG Bulletin, 96(1): 1–22.

Andrews, I.J., 2013. The Carboniferous Bowland Shale Gas Study: Geology and Resource Estimation. British Geological Survey for Department of Energy and Climate Change, London.

Berner, R.A., 1984. Sedimentary pyrite formation: An update. Geochimica et Cosmochimica Acta, 48: 605–615.

Boggs, S., 2006. Principles of Sedimentology and Stratigraphy (4th edition): Pearson Prentice Hall, Upper Saddle River, NJ.

Bomou, B.T., Adatte, T., Tantawy, A.A., Mort, H., Fleitmann, D., Huang, Y., and Föllmi, K.B., 2013. The expression of the Cenomanian–Turonian oceanic anoxic event in Tibet. Paleogeography, Paleoclimatology, Paleoecology, 369: 466–481.

Burton, D., Woolf, K., and Sullivan, B., 2014. Lacustrine depositional environments in the Green River Formation, Uinta Basin: Expression in outcrop and wireline logs. AAPG Bulletin, 98(9): 1699–1715.

Cao, Y., Wang, Y., Xu, T., and Mi, L., 2007. Application of the ratio of characteristic elements in provenance analysis: A case study from the upper part of the fourth member of the Shahejie Fm. in the W58 area, Dongying Depression. Acta Sedimentologica Sinica, 25: 230–238 (in Chinese with English abstract).

Chamberlain, C.P.,Wan, X., Graham, S.A., Carroll, A.R., Doebbert, A.C., Sageman, B.B., Peter, B., Malinda, L.K., Zhou,W., and Chengshan, W., 2013. Stable isotopic evidence for climate and basin evolution of the Late Cretaceous Songliao basin, China. Paleogeography, Paleoclimatology, Paleoecology, 385: 106–124.

Charpentier, R., and Cook, T., 2011. USGS Methodology for Assessing Continuous Petroleum Resources: Geological Survey Open-File Report, 2011-1167.

Curtis, J.B., 2002. Fractured shale-gas systems. AAPG Bulletin, 86(11): 1921–1938.

Dean, W.E., 1999. The carbon cycle and biogeochemical dynamics in lake sediments. Journal of Palaeolimnology, 21: 375–393.

Dodd, T.J.H., McCarthy, D.J., and Richards, P.C., 2019. A depositional model for deep-lacustrine, partially confined, turbidite fans: Early Cretaceous, North Falkland Basin. Sedimentology, 66(1): 53–80.

El Attar, A., and Pranter, M.J., 2016. Regional stratigraphy, elemental chemostratigraphy, and organic richness of the Niobrara Member of the Mancos Shale, Piceance Basin, Colorado. AAPG Bulletin, 100(3): 345–377.

Fairbanks, M.D., Ruppel, S.C., and Rowe, H., 2016. High resolution stratigraphy and facies architecture of the Upper Cretaceous (Cenomanian–Turonian) Eagle Ford Group, Central Texas. AAPG Bulletin, 100(3): 379–403.

Gautier, D.L., 1986. Cretaceous shales from the western interior of North America: Sulfur/carbon ratios and sulfur-isotope composition. Geology, 14: 225.

Glenn, C.R., and Kelts, K., 1986. Sedimentary rhythms in lake deposits. In: Einsele, G. (ed.), Cycles and Events in Stratigraphy. Spring-Verlag, 188–220.

Graf, J.W., Carroll, A.R., and Smith, M.E., 2015. Lacustrine sedimentology, stratigraphy and stable isotope geochemistry of the Tipton Member of the Green River Formation. In: Smith, M.E., and Carroll, A.R. (eds.), Stratigraphy and Paleolimnology of the Green River Formation, Western USA. Springer, Dordrecht, 31–61.

Han, S., Yu, B., Ruan, Z., Bai, C., Shen, Z., and Löhr, S.C., 2021a. Diagenesis and fluid evolution in the third member of the Eocene Shahejie Formation, Bonan Sag, Bohai Bay Basin, China. Marine and Petroleum Geology, 128: 105003.

Han, W., Zhao, X., Pu, X., Chen, S., Wang, H., Liu, Y., Shi, Z., Zhang, W., and Wu, J., 2021b. Fine-grained rock fabric facies classification and its control on shale oil accumulation: A case study from the Paleogene Kong 2 Member, Bohai Bay Basin. Frontiers of Earth Science, 15: 423–437.

Hao, F., Zhou, X., Zhu, Y., Zou, H., Bao, X., and Kong, Q., 2009. Mechanisms of petroleum accumulation in the Bozhong sub-basin, Bohai Bay Basin, China. Part 1: origin and occurrence of crude oils. Marine and Petroleum Geology, 26: 1528–1542.

Hao, F., Zhou, X., Zhu, Y., and Yang, Y., 2011. Lacustrine source rock deposition in response to co-evolution of environments and organisms controlled by tectonic subsidence and climate, Bohai Bay Basin, China. Organic Geochemistry, 42(4): 323–339.

He, J., Ding, W., Jiang, Z., Li, A., Wang, R., and Sun, Y., 2016. Logging identification and characteristic analysis of the lacustrine organic-rich shale lithofacies: A case study from the Es_3 shale in the Jiyang Depression, Bohai Bay Basin, Eastern China. Journal of Petroleum Science & Engineering, 145: 238–255.

He, J., Ding, W., Jiang, Z., Jiu, K., Li, A., and Sun, Y., 2017. Mineralogical and chemical distribution of the Es_3^L oil shale in the Jiyang Depression, Bohai Bay Basin (E China): Implications for paleoenvironmental reconstruction and organic matter accumulation. Marine and Petroleum Geology, 81: 196–219.

Hu, S.B., O'Sullivan, P.B., Raza, A., and Kohn, B.P., 2001. Thermal history and tectonic subsidence of the Bohai Basin, northern China: A Cenozoic rifted and local pull apart basin. Physics of Earth Planetary Interiors, 126: 221–235.

Huang, C., Wang, H., Wu, Y., Wang, J., Chen, S., Ren, P., Liao, Y., Zhao, S., and Xia, C., 2012. Genetic types and sequence stratigraphy models of Palaeogene slope break belts in Qikou Sag, Huanghua Depression, Bohai Bay Basin, Eastern China. Sedimentary Geology, 26: 65–75.

Jarvie, D.M., Hill, R.J., Ruble, T.E., and Pollastro, R.M., 2007. Unconventional shale-gas systems: The Mississippian Barnett Shale of north–central Texas as one model for thermogenic shale-gas assessment. AAPG Bulletin, 91: 475–499.

Jarvie, D.M., 2012. Shale resource systems for oil and gas: Part 1: Shale-gas resource systems. In: Breyer, J.A. (ed.) Shale Reservoirs—Giant Resources for the 21st Century. AAPG Memoirs, 97: 69–87.

Jiu, K., Ding, W., Huang, W., Zhang, Y., Zhao, S., and Hu, L., 2013. Fractures of lacustrine shale reservoirs, the Zhanhua Depression in the Bohai Bay Basin, eastern China. Marine and Petroleum Geology, 48: 113–123.

Khan, D., Qiu, L., Liang, C., Mirza, K., Rehman, S.U., Han, Y., Hannan, A., Kashif, M., and Kra, K.L., 2021. Genesis and distribution of pyrite in the lacustrine shale: Evidence from the Es_3^x shale of the Eocene Shahejie Formation, Zhanhua Sag, East China. ACS Omega, 7(1): 1244–1258.

Khan, D., Qiu, L., Liang, C., Martizzi, P., Mirza, K., and Liu, J. 2022. Tracing forming mechanism of the sparry calcite growth in the lacustrine shale of east China: A glimpse into the role of organic matter in calcite transformation. Geological Journal, 57(5): 1820–1836.

Koh, D.C., Chae, G.T., Ryu, J.S., Lee, S.G., and Ko, K.S., 2016. Occurrence and mobility of major and trace elements in groundwater from pristine volcanic aquifers in Jeju Island, Korea. Applied Geochemistry, 65: 87–102.

Kuhn, P.P., di Primio, R., Hill, R., Lawrence, J.R., and Horsfield, B., 2012. Three-dimensional modeling study of the low permeability petroleum system of the Bakken Formation. AAPG Bulletin, 96(10): 1867–1897.

Lallier-Vergès, E., Hayes, J.M., Boussafir, M., Zaback, D.A., Tribovillard, N.P., Connan, J., and Bertrand, P., 1996. Productivity-induced sulphur enrichment of hydrocarbon-rich sediments from the Kimmeridge Clay Formation. Chemical Geology, 134: 277–288.

Lazar, O.R., Bohacs, K.M., Macquaker, J.H.S., Schieber, J., and Demko, T.M., 2015. Capturing key attributes of fine-grained sediment rocks in outcrops, cores, and thin sections: Nomenclature and description guidelines. Journal of Sedimentary Research, 85: 230–246.

Li, C., Zhu, X., Zhu, S., Geng, M., Bi, Y., Shu, Q., and Xu, F., 2015. Shale reservoir characteristics of the lower 3rd member of Shahejie Formation, Luojia Area, Zhanhua Sag. Acta Sedimentologica Sinica, 33: 795–808 (in Chinese with English abstract).

Li, Q., You, X., Jiang, Z., Wu, S., and Zhang, R., 2020. The origins of carbonate minerals of a source-controlled lacustrine carbonate succession in the Shulu sag, Bohai Bay Basin: Implications for porosity development and paleoenvironment. Marine and Petroleum Geology, 122: 104673.

Liang, C., Jiang, Z., Yang, Y., and Wei, X., 2012. Shale lithofacies and reservoir space of the Wufeng–Longmaxi Formation, Sichuan Basin, China. Petroleum Exploration and Development, 39: 736–743.

Liang, C., Cao, Y., Jiang, Z., Wu, J., Song, G., and Wang, Y., 2017. Shale oil potential of lacustrine black shale in the Eocene Dongying depression: Implications for geochemistry and reservoir characteristics. AAPG Bulletin, 101: 1835–1858.

Liu, Q., Zhu, X., Yang, Y., Geng, M., Tan, M., Jiang, L., and Chen, L., 2016. Sequence stratigraphy and seismic geomorphology application of facies architecture and sediment-dispersal patterns analysis in the third member of Eocene Shahejie Formation, slope system of Zhanhua Sag, Bohai Bay Basin, China. Marine and Petroleum Geology, 78: 766–784.

Liu, Q., He, L., Yi, Z., and Zhang, L., 2022. Anomalous post-rift subsidence in the Bohai Bay Basin, eastern China: Contributions from mantle process and fault activity. Tectonics, 41: TC006748.

Loucks, R.G., and Ruppel, S.C., 2007. Mississippian Barnett mudstone: Lithofacies and depositional setting of a deep-water mudstone-gas succession in the Fort Worth basin, Texas. AAPG Bulletin, 91(4): 579–601.

Loucks, R.G., Reed, R.M., Ruppel, S.C., and Jarvie, D.M., 2009. Morphology, genesis, and distribution of nanometer-scale pores in siliceous mudstones of the Mississippian Barnett Shale. Journal of Sedimentary Research, 79: 848–861.

Loucks, R.G., Reed, R.M., Ruppel, S.C., and Hammes, U., 2012. Spectrum of pore types and networks in mud rocks and a descriptive classification for matrix related mud rock pores. AAPG Bulletin, 96: 1071–1098.

Lü, D., Song, Y., Shi, L., Wang, Z., Cong, P., and Loon, A.J., 2020. The complex transgression and regression history of the northern margin of the Palaeogene Tarim Sea (NW China), and implications for potential hydrocarbon occurrences. Marine and Petroleum Geology, 112: 104041.

Ma, Y., Fan, M., Lu, Y., Liu, H., Hao, Y., Xie, Z., Liu, Z., Peng, L., Du, X., and Hu, H., 2016. Climate-driven paleolimnological change controls lacustrine mudstone depositional process and organic matter accumulation: Constraints from lithofacies and geochemical studies in the Zhanhua Depression, eastern China. International Journal of Coal Geology, 167: 103–118.

Mansour, A.Y., Wagreich, M., Gentzis, T., Ocubalidet, S.G., Tahoun, S.S., and Elewa, A., 2020. Depositional and organic carbon-controlled regimes during the Coniacian–Santonian event: First results from the southern Tethys (Egypt). Marine and Petroleum Geology, 115: 104285.

Montero-Serrano, J.C., Föllmi, K.B., Adatte, T., Spangenberg, J.E., Tribovillard, N., Fantasia, A., and Suan, G., 2015. Continental weathering and redox conditions during the early Toarcian oceanic anoxic event in the northwestern Tethys: Insight from the Posidonia shale section in the Swiss Jura Mountains. Palaeogeography, Palaeoclimatology, Palaeoecology, 429: 83–99.

Moradi, A.V., Sar, A., and Akkaya, P., 2016. Geochemistry of the Miocene oil shale (Hançili Formation) in the Çank ı r ı - Çorum Basin, Central Turkey: Implications for Paleoclimate conditions, source-area weathering, provenance and tectonic setting. Sedimentary Geology, 341: 289–303.

Murphy, D.H., and Wilkinson, B.H., 1980. Carbonate position and facies distribution in a central Michigan marl lake. Sedimentology, 27: 123–135.

Nichols, G., 2009. Sedimentology and Stratigraphy. Wiley-Blackwell, Chichester, 1–411.

Odabasi, M., Tolunay, D., Kara, M., Falay, E.O., Tuna, G., Altiok, H., Dumanoğlu, Y., Bayram, A., and Elbir, T., 2016. Investigation of spatial and historical variations of air pollution around an industrial region using trace and macro elements in tree components. The Science of the Total Environment, 550: 1010–1021.

Picard, M.D., 1971. Classification of fine-grained sedimentary rocks. Journal of Sedimentary Research, 41: 179–195.

Rimmer, S.M., 2004. Geochemical paleoredox indicators in Devonian–Mississipian black shales, central Appalachian basin (USA). Chemical Geology, 206: 373–391.

Ricken, W., 1996. Bedding rhythms and cyclic sequences as documented in organic carbon-carbonate patterns, Upper Cretaceous, Western Interior, U.S. Sedimentary Geology, 102: 131–154.

Sachsenhofer, R., Popov, S., Akhmetiev, M.A., Bechtel, A., Gratzer, R., Gross, D., Horsfield, B., Rachetti, A., Rupprecht, B., Schaffar, W.B., and Zaporozhets, N.I., 2017. The type section of the Maikop Group (Oligocene–lower Miocene) at the Belaya River (North Caucasus): Depositional environment and hydrocarbon potential. AAPG Bulletin, 101: 289–319.

Schenk, C.J., Charpentier, R.R., Klett, T.R., Tennyson, M.E., Mercier, T.J., Brownfield, M.E., Pitman, J.K., Gaswirth, S.B., and Leathers-Miller, H.M., 2015. Assessment of shale-oil resources of the Central Sumatra Basin, Indonesia, 2015. Reston, Virginia, US Geological Survey Fact Sheet 2015–3072, 2 p.

Schieber, J., 2016. Experimental testing of the transport-durability of shale lithics and its implications for interpreting the rock record. Sedimentary Geology, 331: 162–169.

Scholle, P.A., Bebout, D.G., and Moore, C.H., 1983. Carbonate depositional environments. AAPG Memoir, 33: 1–708.

Smith, M.E., Carroll, A.R., 2015. Introduction to the Green River Formation. In: Smith, M.E., and Carroll, A.R. (eds.), Stratigraphy and Paleolimnology of the Green River Formation, Western USA. Springer, Dordrecht, 1–12.

Song, Y., Hu, S., Xu, J., Shen, C., Li, S., Su, P., and Xie, W., 2020. Lacustrine environmental evolution and implications on source rock deposition in the Upper Cretaceous–Paleocene of the South Yellow Sea Basin, off shore eastern China. Marine and Petroleum Geology, 113: 104135.

Tao, S., Xu, Y., Tang, D., Xu, H., Li, S., Chen, S., Liu, W., Cui, Y., and Gou, M., 2017. Geochemistry of the Shitoumei oil shale in the Santanghu Basin, Northwest China: Implications for paleoclimate conditions, weathering, provenance and tectonic setting. International Journal of Coal Geology, 184: 42–56.

Taylor, K.G., and Macquaker, J.H.S., 2014. Diagenetic alterations in a silt- and clay- rich mudstone succession: An example from the Upper Cretaceous Mancos Shale of Utah, USA. Clay Minerals, 49: 213–227.

Tenger, Liu, W., Xu, Y., Chen, J., Hu, K., and Gao, C., 2006. Comprehensive geochemical identification of highly evolved marine hydrocarbon source rocks: Organic matter, paleoenvironment and development of effective hydrocarbon source rocks. Chinese Journal of Geochemistry, 25: 333–340.

Tonger, L., 2004. The discussion on anoxic environments and its geochemical identifying indices. Acta Sedimentologica Sinica, 22: 365–372.

Vasconcelos, C., and McKenzie, J.A., 1997. Microbial mediation of modern dolomite precipitation and diagenesis under anoxic conditions (Lagoa Vermelha, Rio de Janeiro, Brazil). Journal of Sedimentary Research, 67: 378–390.

Wang, Y., Li, M., Pang, X., Zhang, S., and Shi, D., 2005. Fault-fracture mesh petroleum plays in the Zhanhua Depression, Bohai Bay Basin: Part 1. Source rock characterization and quantitative assessment. Organic Geochemistry, 36: 183–202.

Wang, M., Wilkins, R.W., Song, G., Zhang, L., Xu, X., Li, Z., and Chen, G., 2015a. Geochemical and geological

characteristics of the Es_3^L lacustrine shale in the Bonan sag, Bohai Bay Basin, China. International Journal of Coal Geology, 138: 16–29.
Wang, Z., Fu, X., Feng, X., Song, C., Wang, D., Chen, W., and Zeng, S., 2015b. Geochemical features of the black shales from the Wuyu Basin, southern Tibet: Implications for palaeoenvironment and palaeoclimate. Geological Journal, 52 (2): 282–297.
Warren, J., 2000. Dolomite: Occurrence, evolution and economically important associations. Earth-Science Reviews, 52(1): 1–81.
Wilkin, R., Barnes, H.L., and Brantley, S., 1996. The size distribution of framboidal pyrite in modern sediments: An indicator of redox conditions. Geochimica et Cosmochimica Acta, 60: 3897–3912.
Xu, J., Liu, Z., Bechtel, A., Meng, Q., Sun, P., Jia, J., Cheng, L., and Song, Y., 2015. Basin evolution and oil shale deposition during Upper Cretaceous in the Songliao Basin (NE China): Implications from sequence stratigraphy and geochemistry. International Journal of Coal Geology, 149: 9–23.
Yang, W., Jiang, Y., and Wang, Y., 2015. Study on shale facies sedimentary environment of lower Es_3–upper Es_4 in Dongying Sag. Journal of China University of Petroleum (Edition of Natural Science), 39: 19–26.
Yu, Y., Zhang C., Li, S., Zhu, R., Du, J., and Wang, L., 2014. Geochemical characteristics and geological significance of mudstones from Zhujiang Formation of Huizhou depression. Journal of China University of Petroleum, 38: 40–49.
Zhang, S.W., Zhang, L.Y., Bao, Y.S., Li, X.Y., Liu, Q., Li, J.Y., Yin, Y., Zhu, R.F., and Zhang, S.C., 2012. Formation fluid characteristics and hydrocarbon accumulation in the Dongying sag, Shengli oilfield. Petroleum Exploration and Development, 39: 423–435.
Zhang, M., Liu, Z., Xu, S., Sun, P., and Hu, X., 2013. Element response to the ancient lake information and its evolution history of argillaceous source rocks in the Lucaogou Formation in Sangonghe area of southern margin of Junggar Basin. Journal of Earth Science, 24: 987–996.
Zhu, G., Jin, Q., Zhang, S., Dai, J., Wang, G., Zhang, L., and Li, J., 2005. Characteristics and origin of deep lake oil shale of the Shahejie Formation of Paleogene in Dongying Sag, Jiyang Depression. Journal of Palaeogeography, 7: 59–69.
Zhu, X.M., Zhang, S.P., Han, X.F., and Tao, W.F., 2013. On the differences of reservoir quality of Shahejie Formation in steep slope zones of Jiyang Sag. Acta Sedimentologica Sinica, 31 (6): 1094–1104 (in Chinese with English abstract).

About the first author

Danish KHAN, male; born in Pakistan; Ph.D. graduated from School of Geosciences, China University of Petroleum, Qingdao, China. He is interested in fine-grained sedimentology, carbonate sedimentology, diagenesis and reservoir quality prediction. He is currently working as a postdoctoral researcher at State Key Laboratory of Ore Deposit Geochemistry, Institute of Geochemistry, Chinese Academy of Sciences, Guiyang China. E-mail: danish20124@yahoo.com.

About the corresponding authors

LIANG Chao, male, is the professor and doctoral supervisor of the School of Geosciences, China University of Petroleum, Qingdao, China. His research focuses on shale sedimentology, sequence stratigraphy, shale diagenesis and shale reservoir quality prediction. E-mail: liangchao0318@163.com.

QIU Longwei, male, is the professor and doctoral supervisor of the School of Geosciences, China University of Petroleum, Qingdao, China. His research focuses on sequence stratigraphy, sedimentology, reservoir geology and special lithology reservoirs. E-mail: qiulwsd@163.com.